Solid-state photochromic arylazopyrazole based transition metal complexes

Debapriya Gupta,[a,‡] Ankit Kumar Gaur,[a,‡] Deepanshu Chauhan,[b,‡] Sandeep Kumar Thakur,[a,‡] Vaitheesh Jeyapalan,[a,c] Sanjay Singh,*[,a] Gopalan Rajaraman,*[,b] and Sugumar Venkataramani*[,a]

[a]*Department of Chemical Sciences, Indian Institute of Science Education and Research (IISER) Mohali, Sector 81, SAS Nagar, Knowledge City, Manauli -140 306, Punjab, INDIA.*

[b]*Department of Chemistry, Indian Institute of Technology Bombay (IITB), Powai, Mumbai – 400 076, Maharashtra, INDIA.*

[c]*(presently) University of Miami, USA.*

E-mail: sanjaysingh@iisermohali.ac.in, sugumarv@iisermohali.ac.in & rajaraman@chem.iitb.ac.in

S1. General methods:

Reagents and solvents: All the reagents (AR or LR grade) and solvents were purchased from commercially available sources such as Sigma Aldrich, Merck, Avra, Rankem, Spectrochem, and TCI, etc., and used without further purification. For reactions under anhydrous condition, oven dried glasswares have been used under inert atmosphere (N_2 or Ar). Dry solvents such as acetonitrile, etc were obtained from MBraun-SPS solvent purification system. HPLC or UV spectroscopic grade solvents have been used for photoswitching and kinetics studies. For column chromatography, pre-distilled solvents have been utilized.

Chromatography: Thin layer chromatography was performed on Merck Silica gel 60 F$_{254}$ TLC plates, and the plates were visualized using UV chamber (λ = 254 nm). Column chromatography were performed over (100-200 mesh) silica gel and basic alumina.

NMR spectroscopy: ^{1}H and ^{13}C NMR spectra were recorded either in CDCl$_3$, d6-DMSO or CD$_3$CN in Bruker Avance-III 400 MHz spectrometer with operational frequencies 400 and 100 MHz, respectively. All the spectra have been recorded with 16 scans for ^{1}H NMR and 256 scans for ^{13}C NMR. Chemical shift (δ) values are reported in parts per million (ppm) and coupling constants (J) are reported in Hz. Signals of residual solvent signals of CHCl$_3$ (7.26 ppm) and d5-DMSO (2.50 ppm) have been used for internal calibration in ^{1}H NMR, whereas, the spectra have been calibrated using the corresponding signals of CDCl$_3$ (77.16 ppm) and d6-DMSO (39.52 ppm) in ^{13}C NMR. The signal multiplicities are abbreviated as singlet (s), doublet (d), triplet (t), quartet (q), doublet of doublets (dd), doublet of triplets (dt), triplet of doublets (td), doublet of doublet of doublets (ddd), multiplet (m), and broad (br).

HRMS: High resolution mass spectra (HRMS) have been recorded using Waters Synapt G2-Si Q-TOF mass spectrometer. The ionization for those samples has been done using electrospray ionization (ESI) method, and the detections were done in both positive and negative modes.

M. P.: Melting points were recorded on SMP20 melting point apparatus and are uncorrected.

FT-IR studies: FT-IR spectra were recorded as a neat solid or neat liquid on a Bruker Alpha ZnSe ATR spectrometer, or as a KBr pellet on a Perkin Elmer Spectrum Two FTIR spectrometer.

UV-vis spectroscopic studies: UV-vis spectroscopic studies in the solution state have been carried out using an Agilent Cary 5000 UV-Vis NIR spectrophotometer or Agilent Cary 60 UV-Vis spectrophotometer at 1 nm resolution using quartz cuvettes. UV-Vis spectroscopic studies in the solid state have been carried out in the Agilent Cary 5000 UV-Vis NIR spectrophotometer using a Diffuse Reflectance Accessory (DRA) in the KBr medium.

Photoswitching studies and light sources: The analysis of photoswitching, and kinetics measurements have been carried out using an Agilent Cary 5000 UV-Vis NIR spectrophotometer or Agilent Cary 60 UV-Vis spectrophotometer or Bruker Avance-III 400 MHz NMR spectrometer. For forward isomerization step (*EE* to *ZZ*), samples were irradiated (in a quartz cuvette or quartz NMR tube) at 365 nm by using a LED light source (Convoy S2+, 365 nm, 40 mW, a handheld commercial UV light source). The reverse isomerization (*ZZ* to *EE*) has been induced by using 470 nm and 490 nm SX-20 LED light source from Applied Photophysics. PSS has been established by irradiating the sample for prolonged time such that no further spectral changes are observed. For estimation of PSS composition, the samples have been irradiated in a quartz tube (NMR) or cuvette (UV-Vis) using the above-mentioned light sources, and then immediately transferred to the spectrometers for measurement.

Single Crystal X-Ray Diffraction studies: Single crystal X-ray diffraction data were collected using a Rigaku XtaLAB mini diffractometer equipped with a Mercury375M CCD detector. (For details, see section S3).

Elemental Analysis studies: Samples for elemental analysis were analyzed using Elementar Microvario Cube with fully automated PC controlled Elemental Analyser.

Electrochemical studies:

CHI-610 electrochemical workstation from CH Instruments (USA) was used for performing electrochemical studies. The setup consists of a conventional three electrode single-compartment cell consisting of a glassy carbon as the working electrode, Ag/AgCl containing 1M KCl solution as the reference electrode, Pt wire as the counter electrode. Ferrocene was used for internal calibration. Cyclic voltammetry measurements were performed at a scan-rate of 0.1 V/s. 0.1 mol.dm^{-3} tetrabutylammonium hexafluorophosphate dissolved in dry CH_3CN was used as supporting electrolyte. Prior to each measurement, the solutions were purged with nitrogen and the electrochemical potential was internally calibrated against the standard ferrocene/ferrocenium (Fc/Fc$^+$) redox couple.

S2. Synthesis:

Synthesis of *bis*(2-(3,5-dimethyl-4-((*E*)-phenyldiazenyl)-1H-pyrazol-1-yl)ethyl)amine (L1)
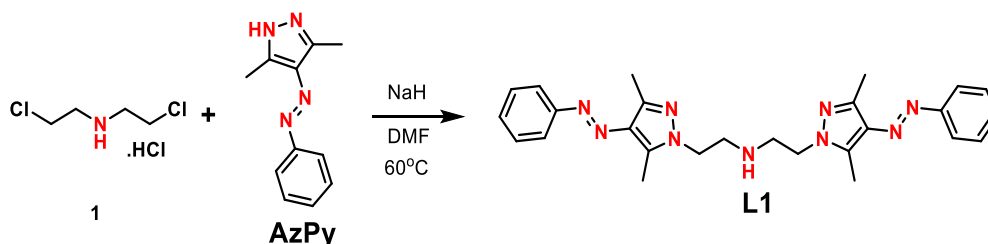
This was prepared according to a slightly modified version of a reported procedure. [1]

A sample of phenylazo-3,5-dimethylpyrazole **AzPy** (1 mmol, 200 mg) was added to 5 ml of anhydrous DMF. The mixture was stirred at rt while sodium hydride (1 mmol, 60% suspension, 40 mg) was added to the mixture pinch wise over a period of half an hour under nitrogen. After stirring this mixture at rt for two hours, *bis*(2-chloroethyl)amine hydrochloride **1** (0.33 mmole, 59 mg) was added and stirred at 60 °C for four hours under nitrogen atmosphere. After checking TLC for completion of the reaction, the reaction mixture was quenched with water. After extracting the mixture multiple times with ethyl acetate, the combined organic layers were dried over anhydrous sodium sulfate and distilled under vacuum. The crude product was eventually purified by column chromatography over 100:200 mesh silica gel using a 1:1 mixture of hexane: ethyl acetate to give the pure product **L1**.

Yellow solid, mp = 56-57 °C, Yield: 60%,^{1}H NMR (400 MHz, d6-DMSO): δ 2.33 (s, 6H), 2.50 (s, 6H; merged), 2.90 (t, *J* = 5.8 Hz, 4H), 4.05 (t, *J* = 5.7 Hz, 4H), 7.40 (t, *J* = 7.1 Hz, 2H), 7.47 (t, *J* = 7.6 Hz ,4H), 7.67 (d, *J*=7.8 Hz, 4H) ppm; ^{13}C (100 MHz, CDCl$_3$): δ 10.0, 14.2, 48.8, 48.9, 121. 9, 129.0, 129.4, 135.1, 139.4, 142.9, 153.7 ppm; HRMS-ESI: *m/z* C$_{26}$H$_{31}$N$_9$ [M+H]$^+$ calc. 470.2780, obs. 470.2794; IR (ATR, cm^{-1}): 590, 681, 761, 1416, 1503, 1553, 1658, 3240.

Synthesis of 2-(3,5-dimethyl-4-((*E*)-phenyldiazenyl)-1H-pyrazol-1-yl)-N-(2-(3,5-dimethyl-4-((*E*)-phenyldiazenyl)-1*H*-pyrazol-1-yl)ethyl)-*N*-methylethan-1-amine (L2)

2-chloro-*N*-(2-chloroethyl)-*N*-methyl-ethanamine hydrochloride was prepared following a literature method. [2]
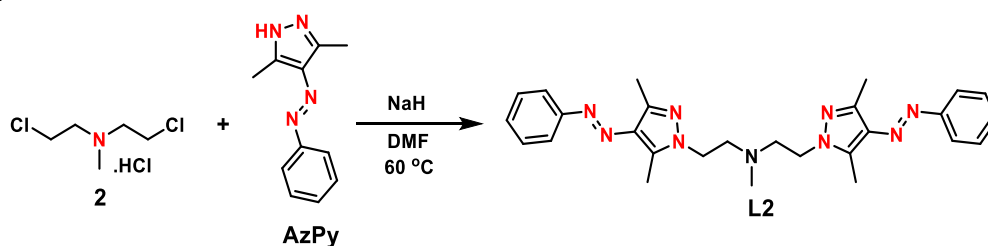
A sample of phenylazo-3,5-dimethylpyrazole **AzPy** (1 mmol, 200 mg) was dissolved in 5 ml of anhydrous DMF under nitrogen atmosphere and stirred at rt. To this sodium hydride (1 mmol, 60% suspension in hexane, 40 mg) was added to it pinch wise over a period of half an hour. After finishing the addition, the mixture was again stirred at rt for a further two hours and then 2-chloro-*N*-(2-chloroethyl)-*N*-methyl-ethanamine hydrochloride **2** (0.33 mmol, 64 mg) was added to it and the mixture was stirred at 60 °C for four hours under nitrogen atmosphere. After checking TLC for the completion of reaction, the reaction mixture was quenched with water. After extracting the mixture multiple times with ethyl acetate, the combined organic layers were dried over anhydrous sodium sulfate and distilled under vacuum. The crude product was eventually purified by column

chromatography over 100:200 mesh silica gel using a 1:2 mixture of hexane: ethyl acetate to give an orange-coloured dense liquid.

Orange-coloured viscous liquid, Yield 65%, ^{1}H NMR (400 MHz, d6-DMSO): δ 2.31 (s, 3H), 2.35 (s, 6H), 2.50 (s, 6H; merged), 2.79 (t, J = 6.2 Hz, 4H), 4.05 (t, J = 6.3 Hz, 4H), 7.40 (t, J = 7.1 Hz, 2H), 7.47 (t, J = 7.2 Hz ,4H), 7.67 (d, J=7.5 Hz, 4H) ppm; [13]C (100 MHz, CDCl$_3$): δ 10.0, 14.2, 43.0, 47.4, 57.4, 121.9, 129.0, 129.4, 135.1, 139.3, 142.7, 153.7 ppm; HRMS-ESI: m/z C$_{27}$H$_{33}$N$_9$ [M+H]$^+$ calc. 484.2937, obs. 484.2953; IR (ATR, cm^{-1}): 685, 699, 763, 996, 1019, 1412, 1504, 1533, 2808, 2850, 2923, 2953, 3064.

Synthesis of 2-(3,5-dimethyl-4-((*E*)-phenyldiazenyl)-1*H*-pyrazol-1-yl)-N-(2-(3,5-dimethyl-4-((*E*)-phenyldiazenyl)-1*H*-pyrazol-1-yl)ethyl)-*N*-(pyridin-2-ylmethyl)ethan-1-amine (L3)[3]
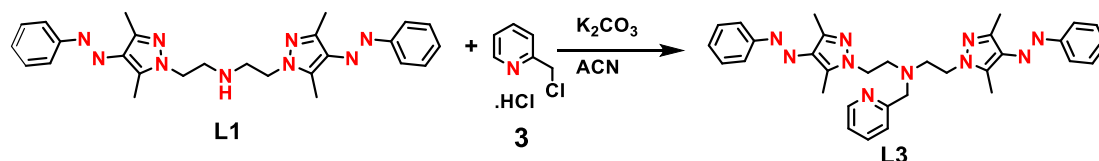
To the ligand **L1** (1 mmol, 470 mg) in anhydrous acetonitrile (8 ml) under nitrogen atmosphere, K$_2$CO$_3$ (2.5 mmol, 345 mg) and 2-(chloromethyl)pyridine hydrochloride (1 mmol, 164 mg) were added and refluxed for 48 hours. After checking TLC for completion of the reaction, the reaction mixture was quenched by adding water. After extracting the mixture multiple times with ethyl acetate, the combined organic layers were dried over anhydrous sodium sulfate and distilled under vacuum. The crude product was then purified by column chromatography over neutral alumina using 1:3 mixture of ethyl acetate: hexane to give an orange-coloured dense liquid.

Orange-coloured viscous liquid, Yield 50%, ^{1}H NMR (400 MHz, d6-DMSO): δ 2.34 (s, 6H), 2.50 (s, 6H; merged), 2.95 (t, J = 6.1 Hz, 4H), 4.11 (t, J = 6.3 Hz, 4H), 7.10 (d, J = 7.8 Hz, 1H), 7.19-7.22 (m, 1H), 7.40-7.43 (m, 2H), 7.48-7.55 (m, 5H), 7.69-7.71 (m, 4H), 8.45 (m, 1H) ppm; [13]C (100 MHz, CDCl$_3$): δ 10.0, 14.1, 47.3, 54.2, 60.8, 121.9, 122.4, 123.0, 129.0, 129.4, 135.2, 136.7, 139.3, 142.7, 149.2, 153.7, 158.8 ppm; HRMS-ESI: m/z C$_{32}$H$_{36}$N$_{10}$ [M+H]$^+$ calc.561.3202, obs.561.3174; IR (ATR, cm^{-1}): 690, 759, 998, 1033,1407, 2838, 2927, 3063.

L1-Ni: To the solution of NiCl$_2$ · 6H$_2$O (1 mmol, 238 mg) in anhydrous THF (8 ml), a solution of **L1** (1 mmol, 470 mg) in anhydrous THF (5 ml) was added and stirred overnight at rt. Afterwards all the volatiles were removed under vacuo. Single crystals suitable for X-ray diffraction were grown by slow evaporation of a small fraction of the compound in a MeOH: ACN (1:1) solution at 4 °C. Green coloured crystals. However, the bulk sample could not be purified.

L1-Cu: To the solution of Cu(NO$_3$)$_2$ · 3H$_2$O (1 mmol, 242 mg) in anhydrous MeOH (8 ml), a solution of **L1** (1 mmol, 470 mg) in anhydrous MeOH was added and stirred overnight at rt. Afterwards all the volatiles were removed under vacuo. Single crystal suitable for X-ray diffraction was grown by slow evaporation of a small fraction of the same solution at rt. Bulk purity was verified by elemental analysis.
Dark blue coloured crystals, Yield: 88%, IR (ATR, cm^{-1}): 2908, 1507, 1408, 1280, 1019, 773, 700, 645. HRMS-ESI: m/z C$_{26}$H$_{31}$CuN$_{10}$O$_3$ [M-NO$_3$]$^+$ calc.594.1877, obs. 594.1904. Elem. Anal. Calcd. for C$_{26}$H$_{31}$CuN$_{11}$O$_6$: C, 47.52; H, 4.76; N, 23.45. Found: C, 47.24; H, 4.60; N, 23.39.

L2-Co: To the solution of Co(NO$_3$)$_2$· 6H$_2$O (1 mmol, 291 mg) in anhydrous methanol (5 ml), a solution of **L2** (1 mmol, 484 mg) in anhydrous methanol was added and stirred overnight at rt. Afterwards all the volatiles under vacuo. Single crystals suitable for X-ray diffraction were grown by slow evaporation of a solution in ACN at rt. Bulk purity was verified by elemental analysis.

Light orange crystals, Yield: 92%, IR (ATR, cm^{-1}): 1646, 1555, 1517, 1394, 1328, 1311, 1284, 1021, 1008, 762. HRMS-ESI: m/z $C_{27}H_{33}CoN_{10}O_3$ [M-NO$_3$]$^+$ calc. 604.2064, obs. 604.2061. Elem. Anal. Calcd. for $C_{27}H_{35}CoN_{11}O_7$: C, 47.37; H, 5.15; N, 22.51. Found: C, 47.06; H, 5.08; N, 22.38.

L2-Cu: To a solution of $Cu(NO_3)_2 \cdot 3H_2O$ (1 mmol, 242 mg) in anhydrous methanol (5 ml), a solution of **L2** (1 mmol, 484 mg) in anhydrous methanol (5 ml) was added and stirred overnight at rt. Afterwards all the volatiles were removed under vacuo. Single crystals suitable for X-ray diffraction were grown by slow evaporation of a fraction of the same solution at rt. Bulk purity was verified by elemental analysis.

Dark green crystals. Yield: 95%, IR (ATR, cm^{-1}): 1585, 1552, 1498, 1453, 1418, 1369, 1074, 1009, 768, 701. HRMS-ESI: m/z $C_{27}H_{33}ClCuN_9$ [M-Cl]$^+$ calc. 581.1843, obs. 581.1841. Elem. Anal. Calcd. for $C_{27}H_{33}Cl_2CuN_9 \cdot H_2O$: C, 50.98; H, 5.55; N, 19.82. Found: C, 51.23; H, 5.28; N, 19.47.

L2-Ni: To a solution of $Ni(NO_3)_2 \cdot 6H_2O$ (1 mmol, 291 mg) in anhydrous methanol (5 ml), a solution of **L2** (1 mmol, 484 mg) dissolved in anhydrous methanol (5 ml) was added and stirred overnight at rt. Afterwards all the volatiles were removed under vacuo. Single crystals suitable for X-ray diffraction were grown by slow evaporation of an acetonitrile solution of the same at rt, Bulk purity of the product was verified by elemental analysis.
Light green coloured crystals, Yield: 90%, IR (ATR, cm^{-1}): 1479, 1395, 1282, 1024, 1008, 762, 700, 683. HRMS-ESI: m/z $C_{27}H_{33}N_{10}NiO_3$ [M-NO$_3$]$^+$ calc. 603.2091, obs. 603.2127. Elem. Anal. Calcd. for $C_{27}H_{35}N_{11}NiO_7$: C, 47.39; H, 5.16; N, 22.51. Found: C, 47.06; H, 5.08; N, 22.38.

L3-Co: To a solution of $CoCl_2 \cdot 6H_2O$ (1 mmol, 238 mg) in anhydrous methanol (5 ml), a solution of **L3** (1 mmol, 561 mg) and NH_4PF_6 (1 mmole, 163 mg) dissolved in anhydrous methanol was added and stirred overnight at rt. Afterwards all the volatiles were removed under vacuo. Single crystals suitable for X-ray diffraction were grown by slow evaporation of a small fraction of the compound in a methanol: acetonitrile (1:1) solution at 4 °C. Green coloured crystals, Bulk of the sample could not be purified.

L3-Cu: To a solution of $CuCl_2 \cdot 2H_2O$ (1 mmol, 171 mg) in anhydrous methanol (5 ml), a solution of **L3** (1 mmol, 561 mg) and NH_4PF_6 (1 mmol, 163 mg) dissolved in anhydrous methanol was and stirred at rt for 8 hours. Afterwards all the volatiles were removed under vacuo. Single crystals suitable for X-ray diffraction were grown by slow evaporation of MeOH: ACN (1:1) solution at rt. Bulk purity was established by elemental analysis.
Dark green crystal. Yield: 90%, IR (ATR, cm^{-1}): 1611, 1492, 1419, 1323, 1302, 1028, 1000, 832, 768, 707, 687. HRMS-ESI: m/z $C_{32}H_{36}ClCuN_{10}$ [M-PF$_6$]$^+$ calc. 658.2103, obs. 658.2113. Elem. Anal. Calcd. for $C_{32}H_{36}ClCuN_{10}PF_6 \cdot 2H_2O$: C, 45.72; H, 4.80; N, 16.66. Found: C, 45.42; H, 4.49; N, 17.16.

S3: Crystallographic data and refinement details of complexes: -

Single crystal X-ray diffraction data of complexes **L1-Cu**, **L1-Ni**, **L2-Co**, **L2-Cu**, **L2-Ni**, **L3-Co**, **L3-Cu** were collected using a Rigaku XtaLAB mini diffractometer equipped with Mercury375M CCD detector. The data were collected with MoKα radiation (λ = 0.71073 Å) using omega scans. During the data collection, the detector distance was 49.9 mm (constant) and the detector was placed at 2θ = 29.85° (fixed) for all the data sets. The data collection and data reduction were done using CrysAlisPro 1.171.38.46 and all the crystal structures were solved through OLEX2[4] package using SHELXT[5] and the structures were refined using SHELXL[5]. All non-hydrogen atoms were refined anisotropically. All Figures were generated using Mercury 2020.3.0.

Single crystal X-ray structure of complexes L1-Ni and L3-Co

L1–Ni   L3–Co
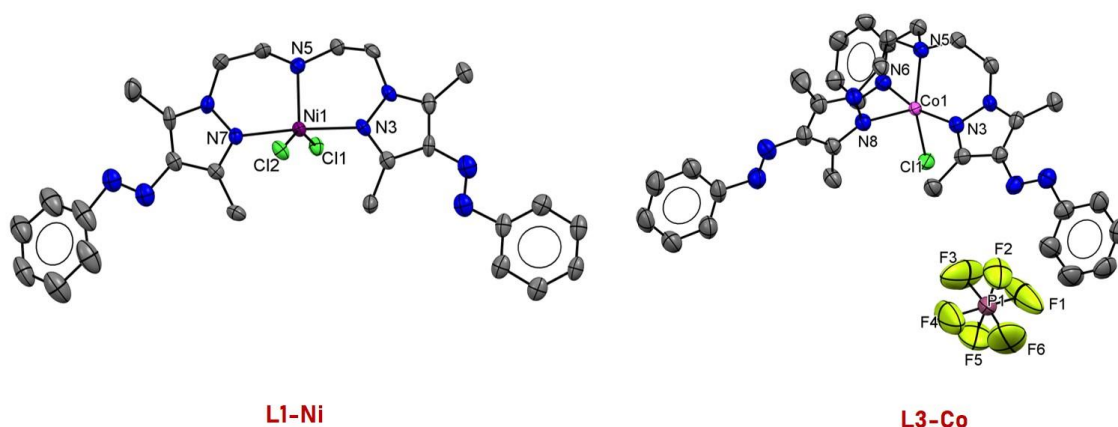
Figure S3-1. Single crystal X-ray structure of complexes **L1-Ni** and **L3-Co**. Thermal ellipsoids are set at 50 % probability. All hydrogen atoms have been omitted for clarity. Selected interatomic distances (Å) and bond angles (°) for **L1-Ni**: Ni1-Cl1 2.3194(15), Ni1-Cl2 2.3325(15), Ni1-N3 2.114(5), Ni1-N5 2.022(5), Ni1-N7 2.097(5); Cl1-Ni1-Cl2 149.30(6), N3-Ni1-Cl1 91.56(13), N3-Ni1-Cl2 90.48(14), N5-Ni1-Cl1 100.42(14), N5-Ni1-Cl2 110.17(14), N5-Ni1-N3 90.93(18), N5-Ni1-N7 93.93(18), N7-Ni1-Cl1 88.10(13), N7-Ni1-Cl2 87.33(14), N7-Ni1-N3 175.11(19). **L3-Co:** Co1-Cl1 2.2732(10), Co1-N3 2.011(3), Co1-N5 2.135(3), Co1-N6 2.008(3), Co1-N8 2.263(3); N3-Co1-Cl1 91.73(9), N5-Co1-Cl1 156.12(9), N5-Co1-N8 96.02(12), N6-Co1-Cl1 92.76(9), N6-Co1-N3 166.22(13), N6-Co1-N5 80.36(12), N6-Co1-N8 93.10(12), N8-Co1-Cl1 107.23(9).

Complex[a]	L1-Cu	L1-Ni	L2-Co	L2-Cu	L2-Ni	L3-Co	L3-Cu
Chemical formula	$C_{26}H_{31}CuN_{11}O_6$	$C_{28}H_{34}Cl_2N_{10}Ni$	$C_{27}H_{35}CoN_{11}O_7$	$C_{28}H_{36}Cl_2CuN_9O$	$C_{27}H_{35}N_{11}NiO_7$	$C_{38}H_{45}ClCoF_6N_{13}P$	$C_{34}H_{39}ClCuF_6N_{11}P$
Molar mass	657.16	640.26	684.59	649.10	684.37	923.22	845.72
Crystal system	Triclinic	Orthorhombic	Orthorhombic	Monoclinic	Orthorhombic	Triclinic	Triclinic
Space group	$P\bar{1}$	$Pbca$	$Pna2_1$	$P2_1/c$	$Pna2_1$	$P\bar{1}$	$P\bar{1}$
T [K]	150.0(10)	100.01(1)	150.00(10)	150.00(10)	150.00(10)	200.00(10)	200.01(10)
a [Å]	12.3869(2)	11.8157(9)	22.7175(6)	8.0819(4)	22.7104(7)	13.3989(3)	9.83040(10)
b [Å]	13.6857(2)	18.6896(14)	8.1843(2)	11.0997(5)	8.1474(3)	13.9625(3)	12.06690(10)
c [Å]	18.1749(3)	57.081(4)	34.2222(8)	35.5600(13)	34.2726(10)	13.9899(3)	16.5603(2)
α [°]	86.6370(10)	90	90	90	90	71.644(2)	104.0100(10)
β [°]	72.859(2)	90	90	92.781(4)	90	79.391(2)	96.3360(10)
γ [°]	85.7820(10)	90	90	90	90	62.288(2)	101.1170(10)
V [Å³]	2934.03(9)	12605.1(16)	6362.8(3)	3186.2(2)	6341.5(4)	2196.95(9)	1844.60(3)
Z	4	16	8	4	8	2	2
D(calcd.) [g·cm⁻³]	1.488	1.350	1.429	1.353	1.434	1.396	1.523
μ(Mo-K_α) [mm⁻¹]	0.806	0.821	0.602	0.890	0.674	0.558	0.782
Reflections collected	41343	62405	57727	23322	46526	31024	41120
Independent reflections	10355	11155	11258	5645	11211	7763	12823
Data/restraints/parameters	10355/0/813	11155/162/707	11258/27/713	5645/6/376	11211 /3/593	7763/0/548	12823/0/492
$R1,wR2[I>2\sigma(I)]$[a]	0.0408, 0.1033	0.0744, 0.1816	0.0739, 0.1877	0.0704, 0.1979	0.0618, 0.1539	0.0618, 0.1650	0.0397, 0.1022
R1, wR2 (all data)[a]	0.0561, 0.1180	0.1127, 0.2145	0.0879, 0.2079	0.0875, 0.2202	0.0729 , 0.1665	0.0765, 0.1807	0.0505, 0.1131
GOF	1.050	1.034	1.034	1.049	1.047	1.047	1.075
CCDC	2149916	2149917	2149918	2149919	2149920	2149921	2149922

[a] $R1 = \Sigma||Fo| - |Fc||/\Sigma|Fo|$. $wR2 = [\Sigma w(|Fo^2| - |Fc^2|)^2/\Sigma w|Fo^2|^2]^{1/2}$

S4. Analysis of photoswitching and thermal stability aspects using UV-Vis spectroscopy in solution and solid state:

Photoswitching studies have been carried out in solution phase (CH_3CN) and solid-state (in KBr medium) and analysed by using UV-vis spectroscopy.
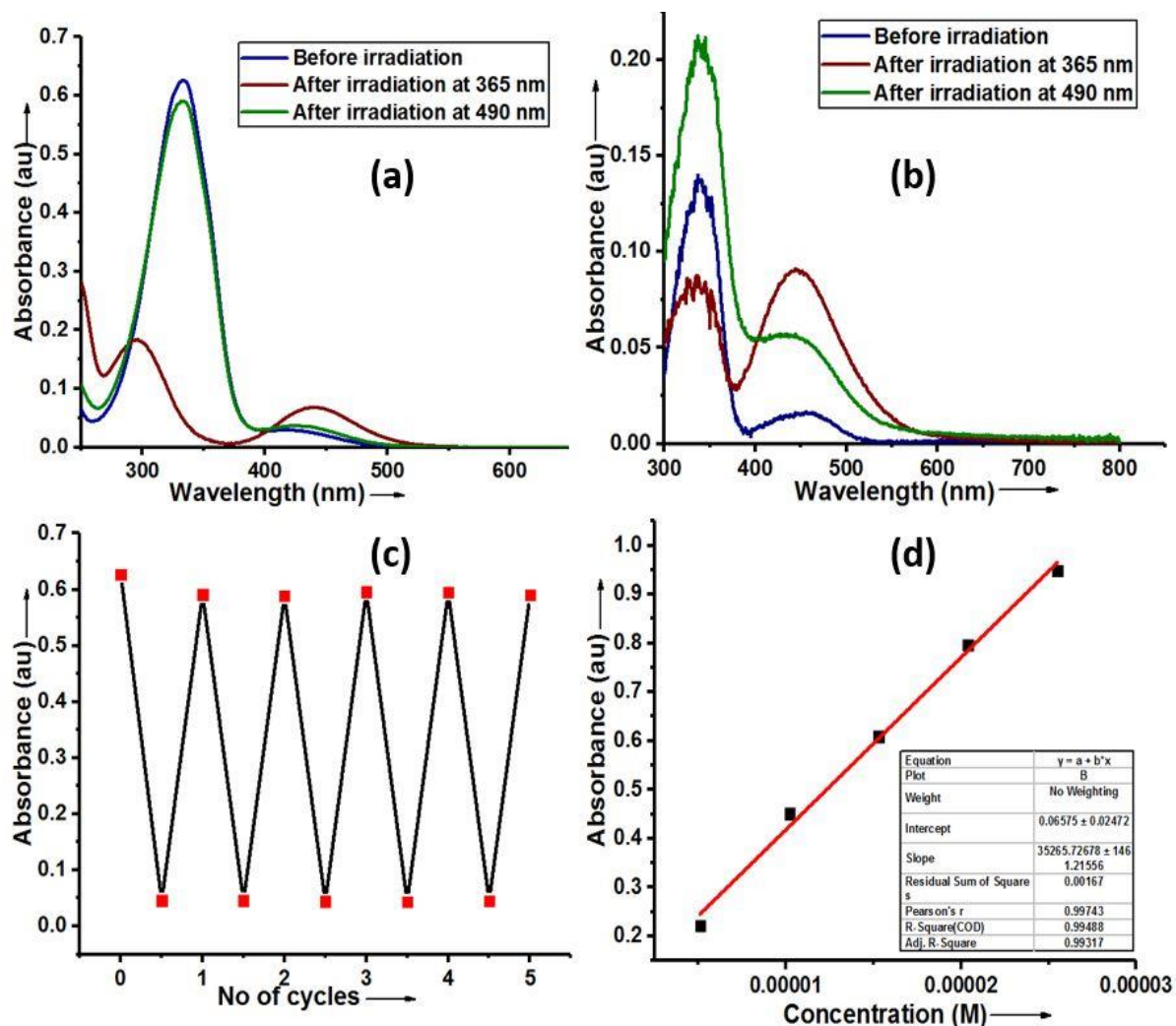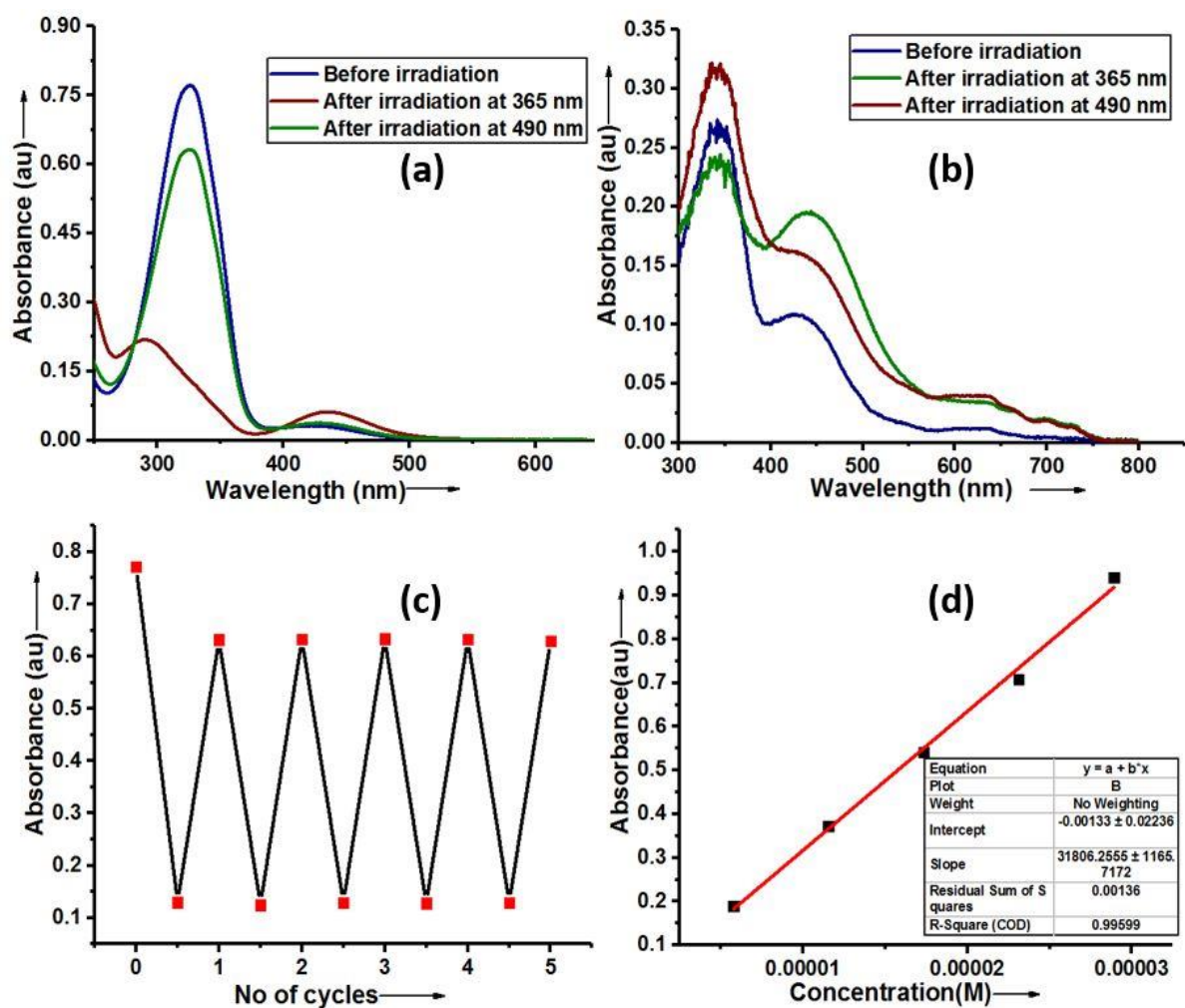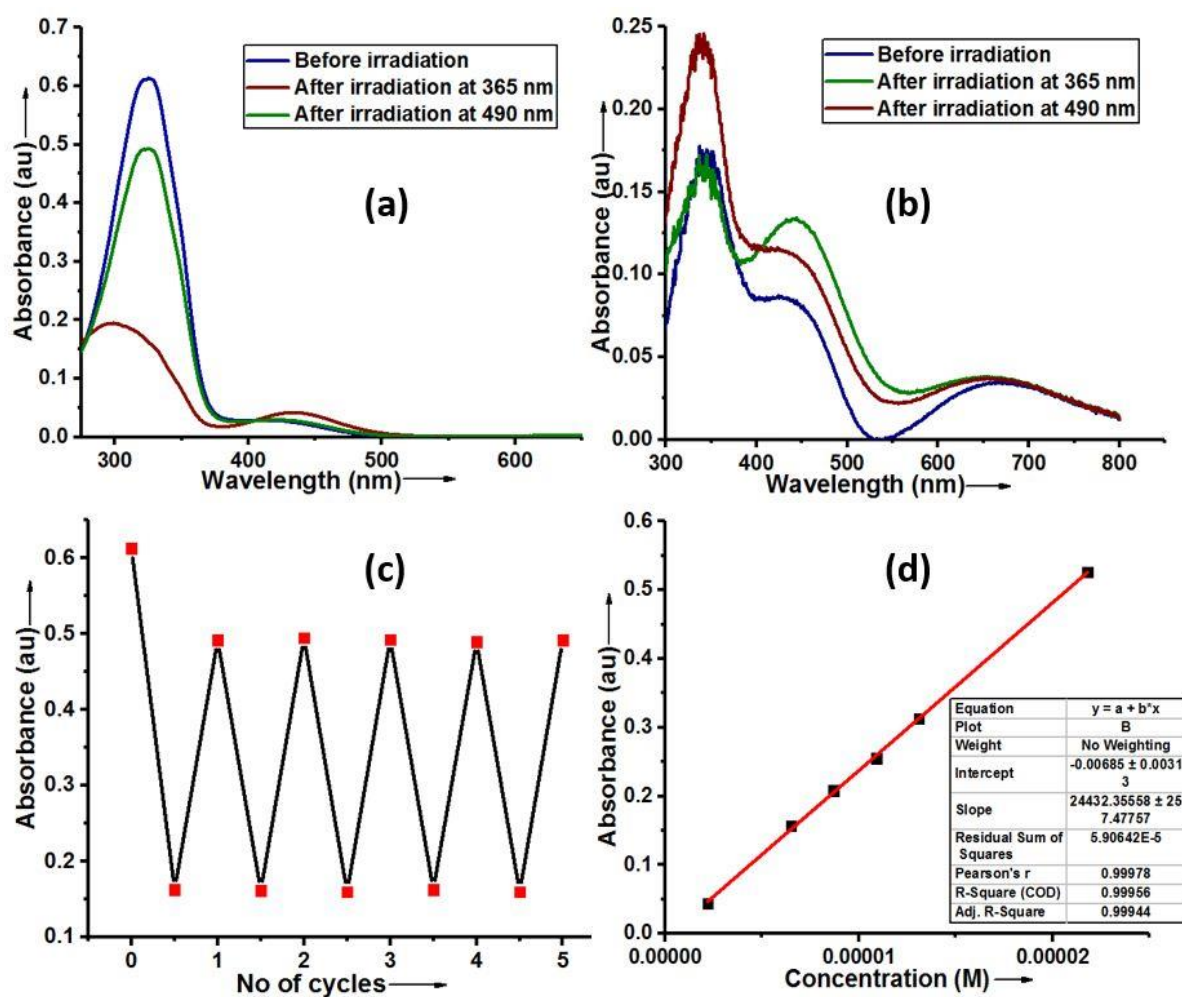

Figure S4-1: Photoswitching behaviour of **L1:** (a) Forward and reverse photoisomerization (CH_3CN, 18 μM); (b) Forward and reverse photoisomerization in solid state (3.5 mg of **L1** diluted with 400 mg KBr); (c) Photoswitching stability test upto five cycles of **L1** in CH_3CN (forward isomerization step: 365 nm; reverse isomerizarion step: 490 nm); (d) Estimation of molar extinction coefficient (in CH_3CN) for the π−π* absorption.
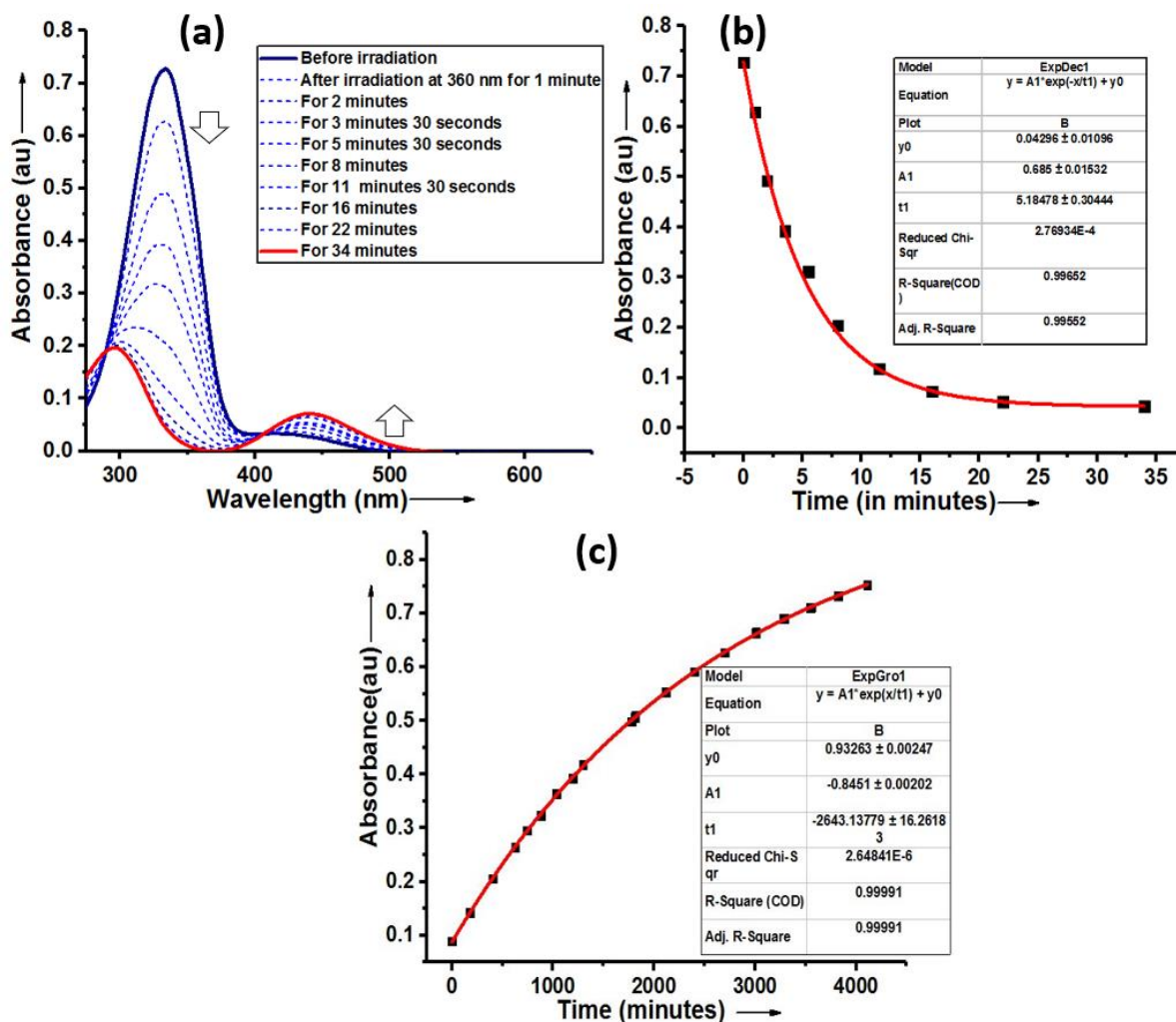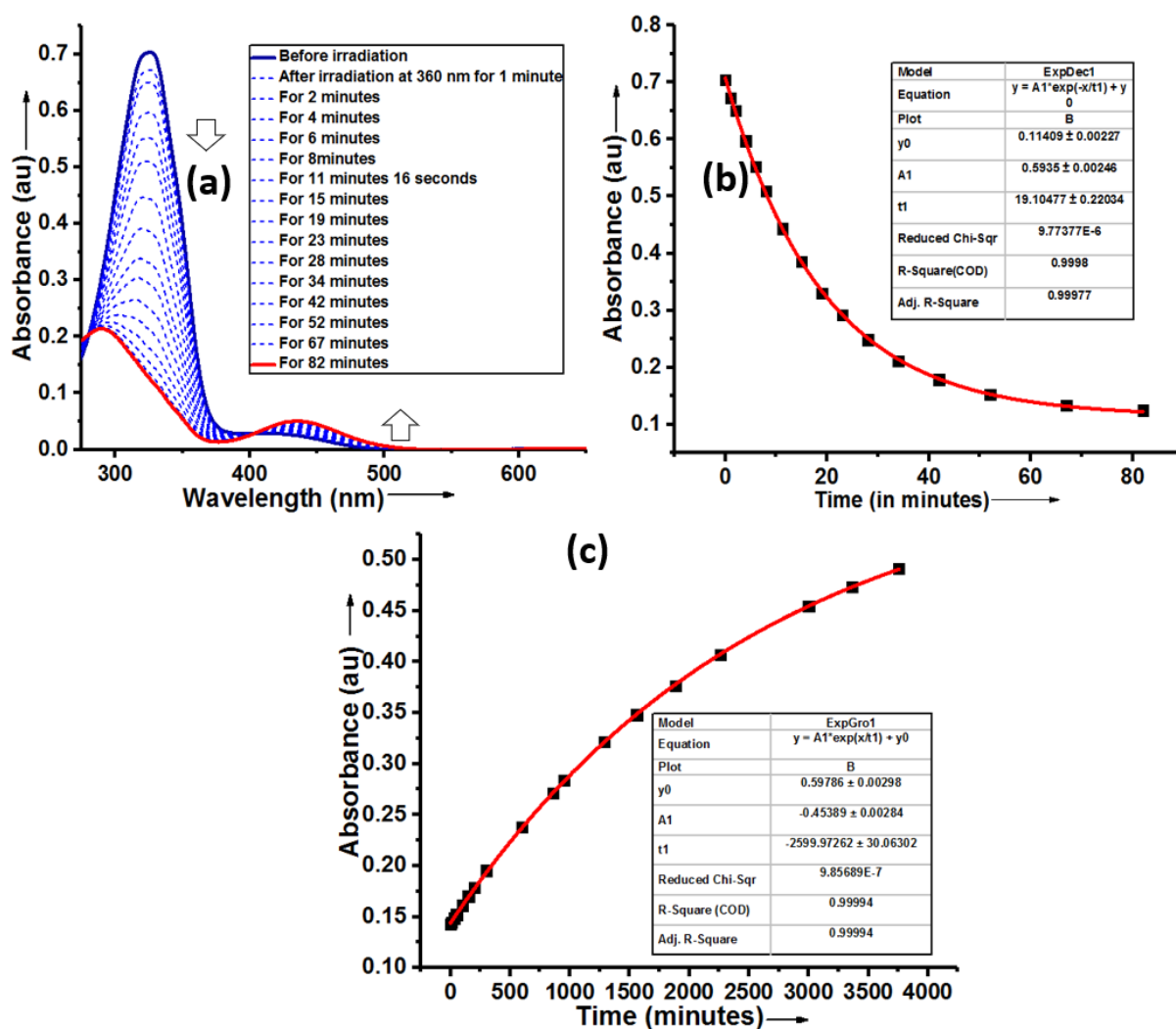
Figure S4-2: Photoswitching and thermal stability aspects of **L1:** (a) Forward isomerization kinetics measurements of **L1** under 360 nm (UV-Vis spectroscopic monitoring of the 20.7 μM solution in CH_3CN at rt; illumination using 100 μW 360 nm LED); (b) Exponential decay plot for the forward isomerisation step (Absorbance at λ_{max} = 334 nm); (c) First order thermal reverse isomerization kinetics plot and exponential fit of **L1** (16 μM in CH_3CN, 40 °C).
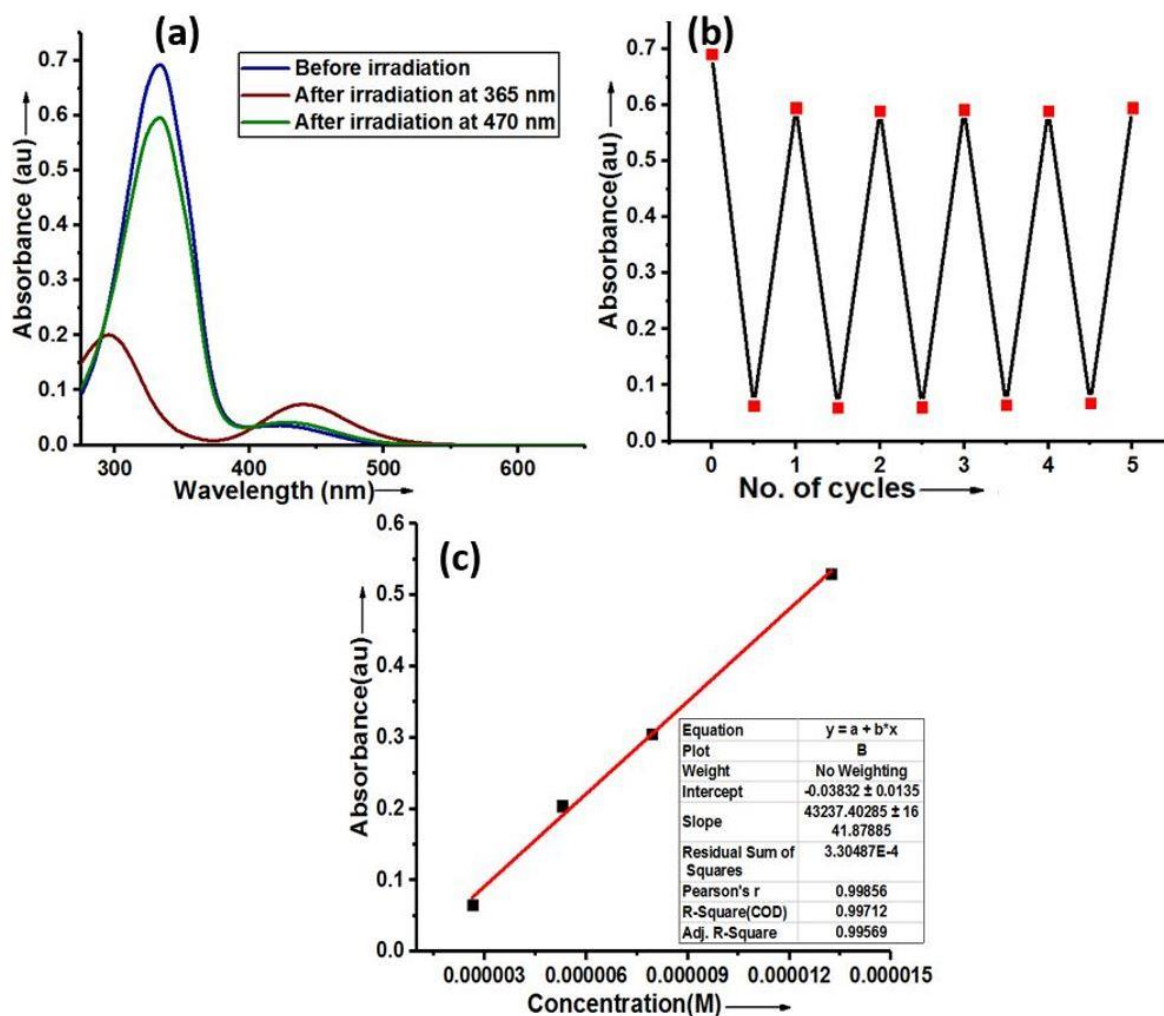
Figure S4-3: Photoswitching behaviour of **L2:** (a) Forward and reverse photoisomerization (CH$_3$CN, 16 µM); (b) Photoswitching stability test upto five cycles of **L2** in CH$_3$CN (forward isomerization step: 365 nm; reverse isomerizarion step: 470 nm); (d) Estimation of molar extinction coefficient (in CH$_3$CN) for the π–π* absorption.

(a)

Legend:
- Before irradiation
- After irradiation at 360 nm for 2 minutes
- For 4 minutes
- For 6 minutes
- For 8 minutes
- For 10 minutes
- For 12 minutes
- For 14 minutes
- For 16 minutes
- For18 minutes
- For 20 minutes

(b)

Model	ExpDec1
Equation	$y = A1*exp(-x/t1) + y0$
Plot	B
y0	0.03706 ± 0.00623
A1	0.60241 ± 0.00824
t1	5.47202 ± 0.20058
Reduced Chi-Sqr	6.59221E-5
R-Square(COD)	0.99854
Adj. R-Square	0.99817

(c)

Model	ExpGro1
Equation	$y = A1*exp(x/t1) + y0$
Plot	Absorbance
y0	1.00934 ± 0.00538
A1	-0.91365 ± 0.00474
t1	-2949.45534 ± 32.70247
Reduced Chi-Sqr	5.61996E-6
R-Square (COD)	0.99989
Adj. R-Square	0.99988

Figure S4-4: Photoswitching and thermal stability aspects of **L2:** (a) Forward isomerization kinetics measurements of **L2** under 360 nm (UV-Vis spectroscopic monitoring of the 17.9 μM solution in CH$_3$CN at rt; illumination using 100 μW 360 nm LED); (b) Exponential decay plot for the forward isomerisation step (Absorbance at λ_{max} = 334 nm); (c) First order thermal reverse isomerization kinetics plot and exponential fit of **L2** (17.8 μM in CH$_3$CN, 40 °C).
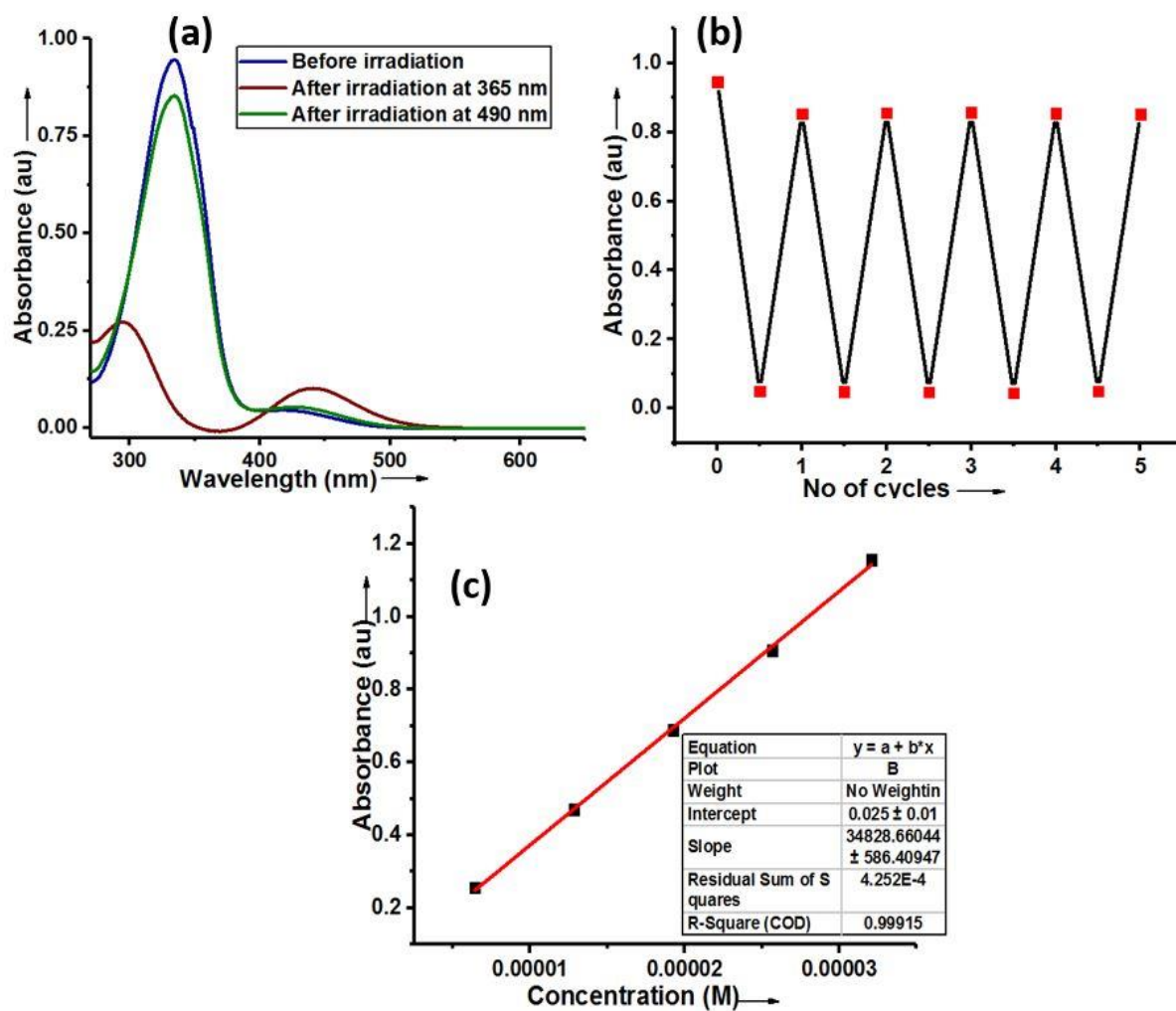
Figure S4-5: Photoswitching behaviour of **L3:** (a) Forward and reverse photoisomerization (CH₃CN, 27 µM); (b) Photoswitching stability test upto five cycles of **L3** in CH₃CN (forward isomerization step: 365 nm; reverse isomerizarion step: 490 nm); (d) Estimation of molar extinction coefficient (in CH₃CN) for the $\pi-\pi^*$ absorption.
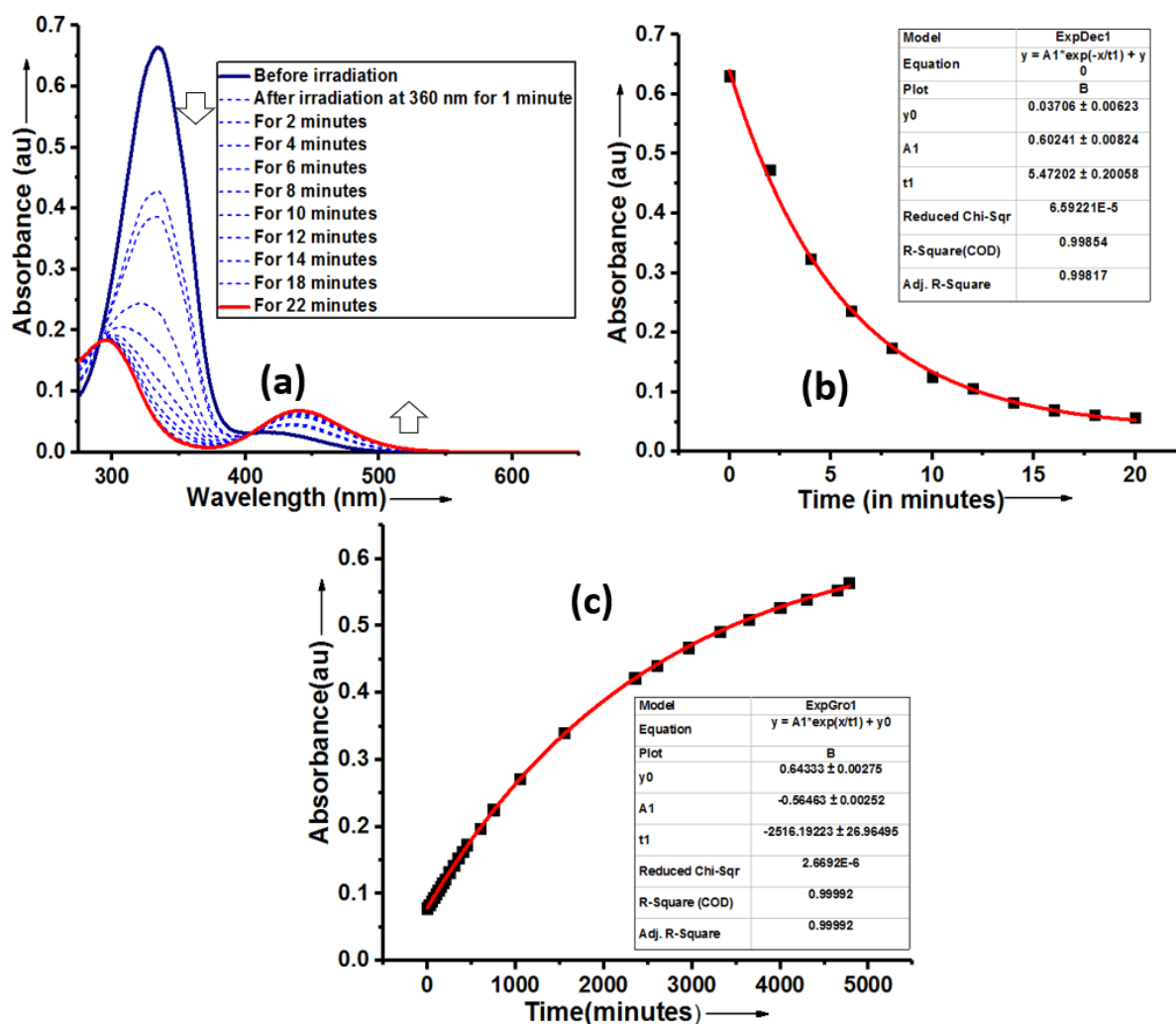
Figure S4-6: Photoswitching and thermal stability aspects of **L3:** (a) Forward isomerization kinetics measurements of **L3** under 360 nm (UV-Vis spectroscopic monitoring of the 19 µM solution in CH₃CN at rt; illumination using 100 µW 360 nm LED); (b) Exponential decay plot for the forward isomerisation step (Absorbance at λ_{max} = 334 nm); (c) First order thermal reverse isomerization kinetics plot and exponential fit of **L3** (16 µM in CH₃CN, 40 °C).
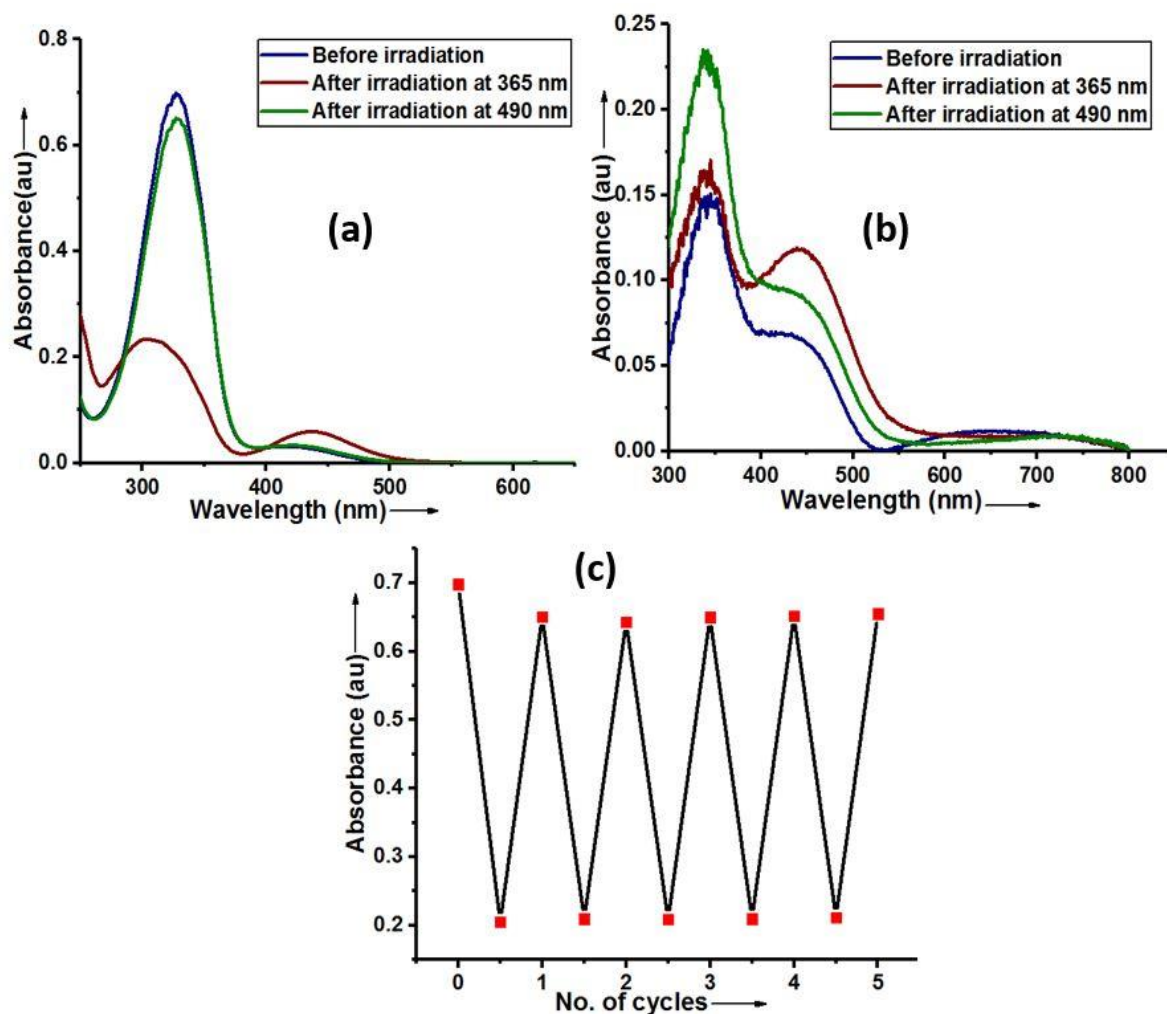
Figure S4-7: Photoswitching behaviour of **L1-Cu:** (a) Forward and reverse photoisomerization (CH₃CN, concentration 15-20µM, exact concentration unknown because of poor solubility); (b) Forward and reverse photoisomerization in solid state (1mg of **L1-Cu** diluted with 1000 mg KBr); (c) Photoswitching stability test upto five cycles of **L1-Cu** in CH₃CN (forward isomerization step: 365 nm; reverse isomerizarion step: 490 nm).
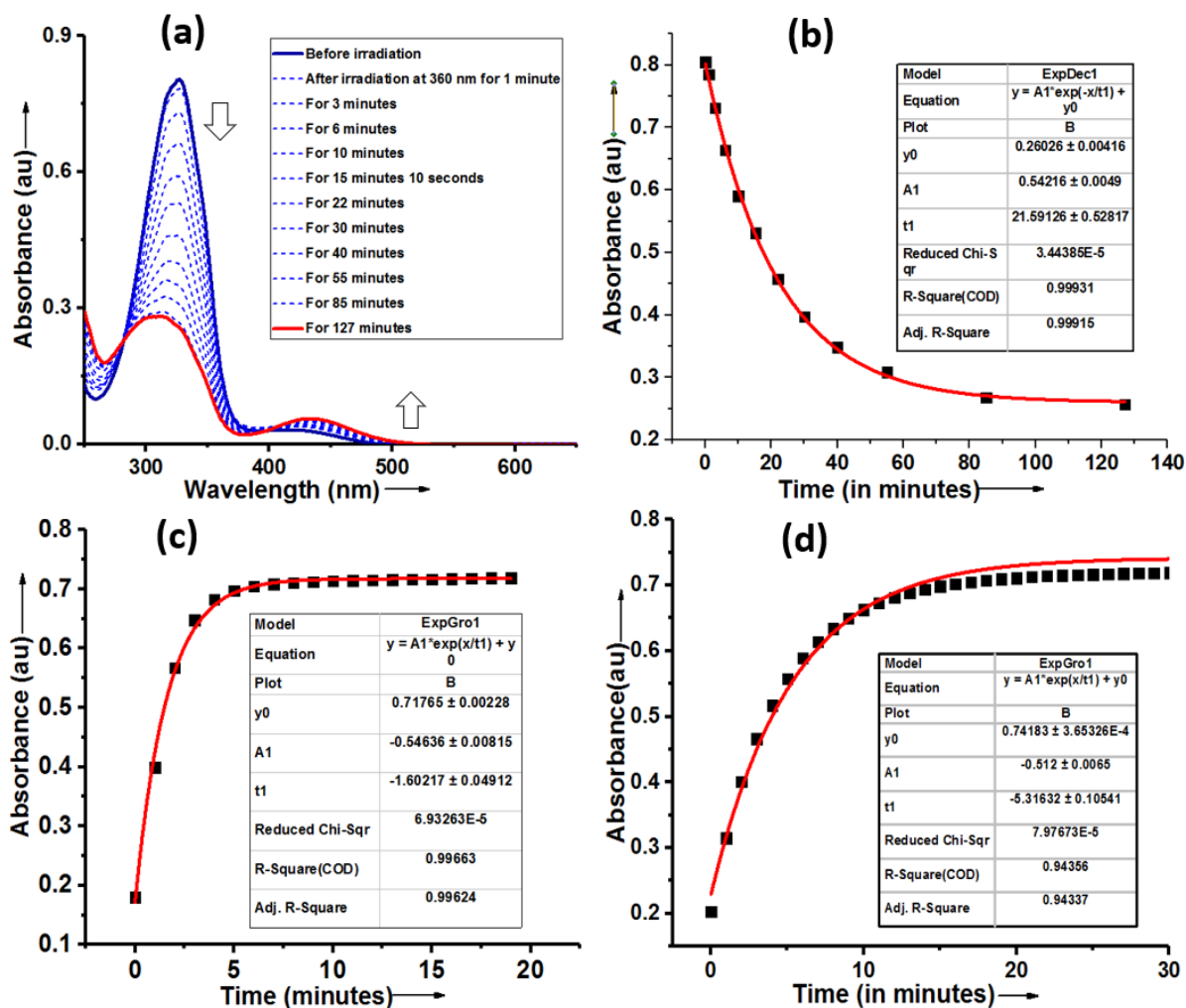
Figure S4-8: Photoswitching and thermal stability aspects of **L1-Cu:** (a) Forward isomerization kinetics measurements of **L1-Cu** under 360 nm (UV-Vis spectroscopic monitoring of approximately 25 μM solution in CH₃CN at rt; illumination using 100 μW 360 nm LED); (b) Exponential decay plot for the forward isomerisation step (Absorbance at λ_{max} = 327 nm); (c) First order thermal reverse isomerization kinetics plot and exponential fit of **L1-Cu** (approximately 20 μM in CH₃CN, 40 °C); (d) First order thermal reverse isomerization kinetics plot and exponential fit of **L1-Cu** (approximately 20 μM in CH₃CN, 25 °C).
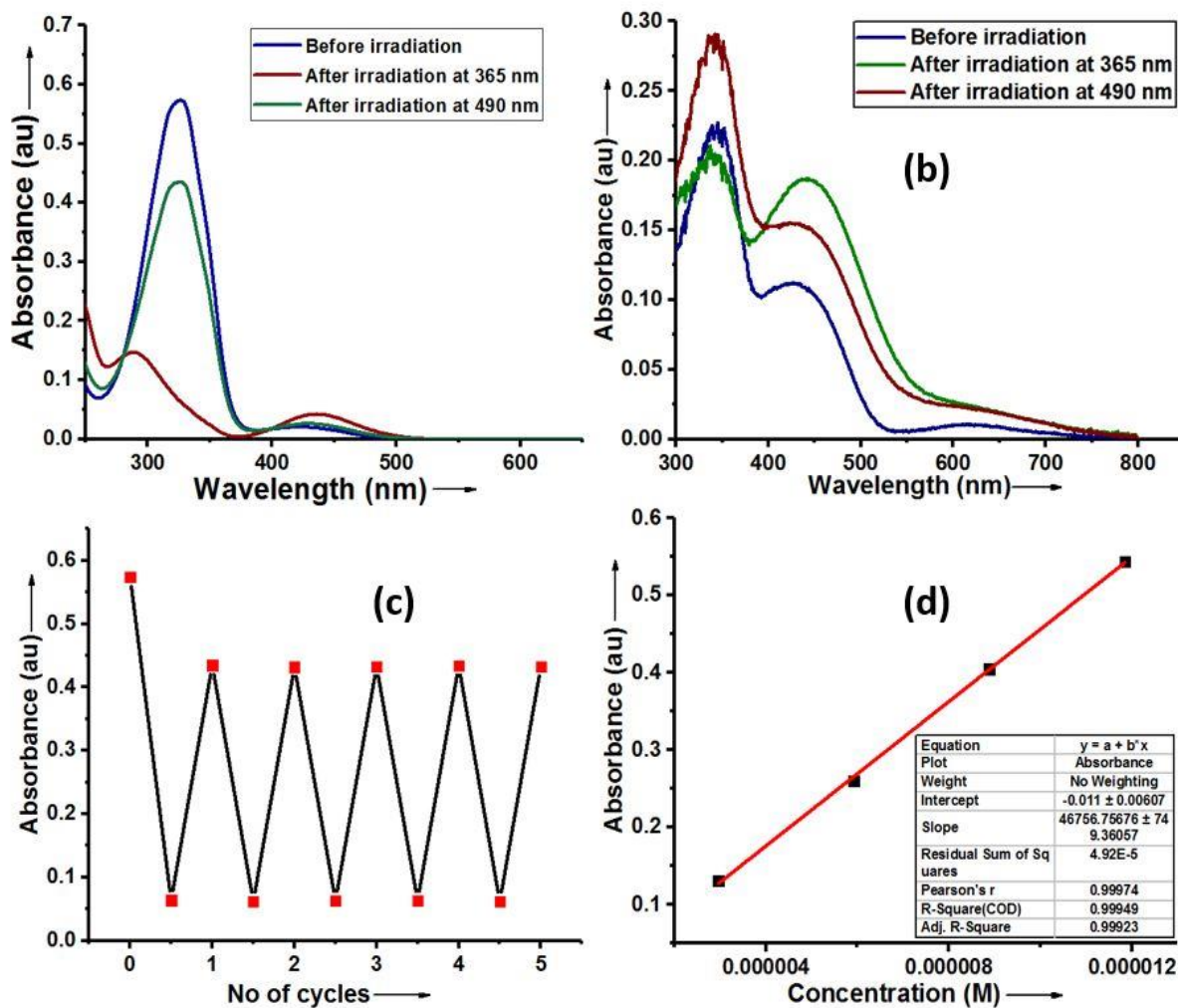
Figure S4-9: Photoswitching behaviour of **L2-Ni:** (a) Forward and reverse photoisomerization (CH₃CN, concentration 12 µM; (b) Forward and reverse photoisomerization in solid state (1 mg of **L2-Ni** diluted with 1200 mg KBr); (c) Photoswitching stability test upto five cycles of **L2-Ni** in CH₃CN (forward isomerization step: 365 nm; reverse isomerizarion step: 490 nm). (d) Estimation of molar extinction coefficient (in Acetonitrile) for the $\pi-\pi^*$ absorption.
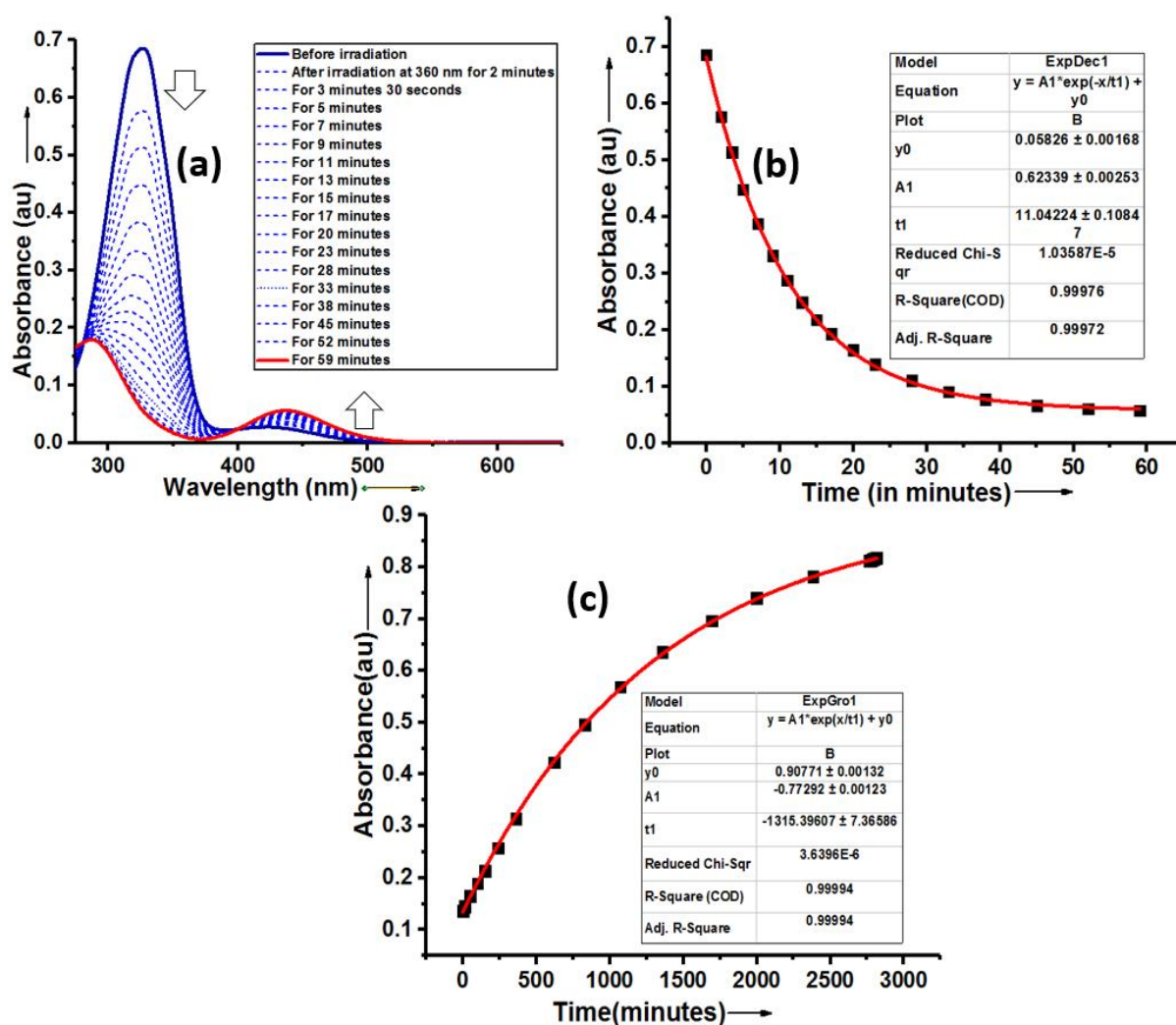
Figure S4-10: Photoswitching and thermal stability aspects of **L2-Ni:** (a) Forward isomerization kinetics measurements of **L2-Ni** under 360 nm (UV-Vis spectroscopic monitoring of approximately 14.6 μM solution in CH$_3$CN at rt; illumination using 100 μW 360 nm LED); (b) Exponential decay plot for the forward isomerisation step (Absorbance at λ$_{max}$ = 326 nm); (c) First order thermal reverse isomerization kinetics plot and exponential fit of **L2-Ni** (17.5 μM in CH$_3$CN, 40 °C).

Figure S4-11: Photoswitching behaviour of **L2-Co:** (a) Forward and reverse photoisomerization (CH₃CN, concentration 24 µM; (b) Forward and reverse photoisomerization in solid state (1 mg of **L2-Co** diluted with 1200 mg KBr); (c) Photoswitching stability test upto five cycles of **L2-Co** in CH₃CN (forward isomerization step: 365 nm; reverse isomerizarion step: 490 nm). (d) Estimation of molar extinction coefficient (in Acetonitrile) for the $\pi-\pi^*$ absorption.
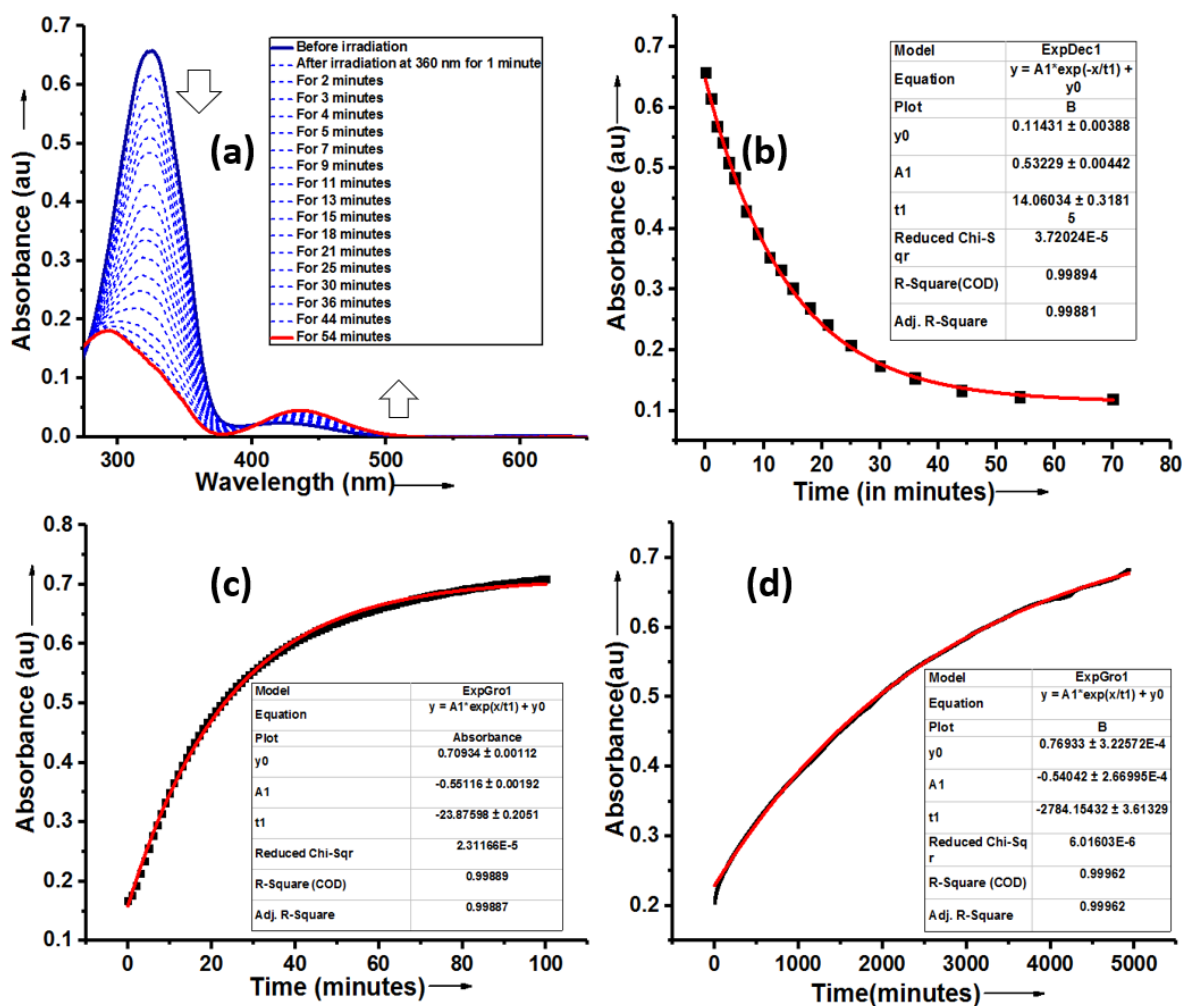
Figure S4-12: Photoswitching and thermal stability aspects of **L2-Co:** (a) Forward isomerization kinetics measurements of **L2-Co** under 360 nm (UV-Vis spectroscopic monitoring of approximately 20.7 μM solution in CH$_3$CN at rt; illumination using 100 μW 360 nm LED); (b) Exponential decay plot for the forward isomerisation step (Absorbance at λ$_{max}$ = 326 nm); (c) First order thermal reverse isomerization kinetics plot and exponential fit of **L2-Co** (22.3 μM in CH$_3$CN, 40 °C); (d) First order thermal reverse isomerization kinetics plot and exponential fit of **L2-Co** (22.3 μM in CH$_3$CN, 25 °C).
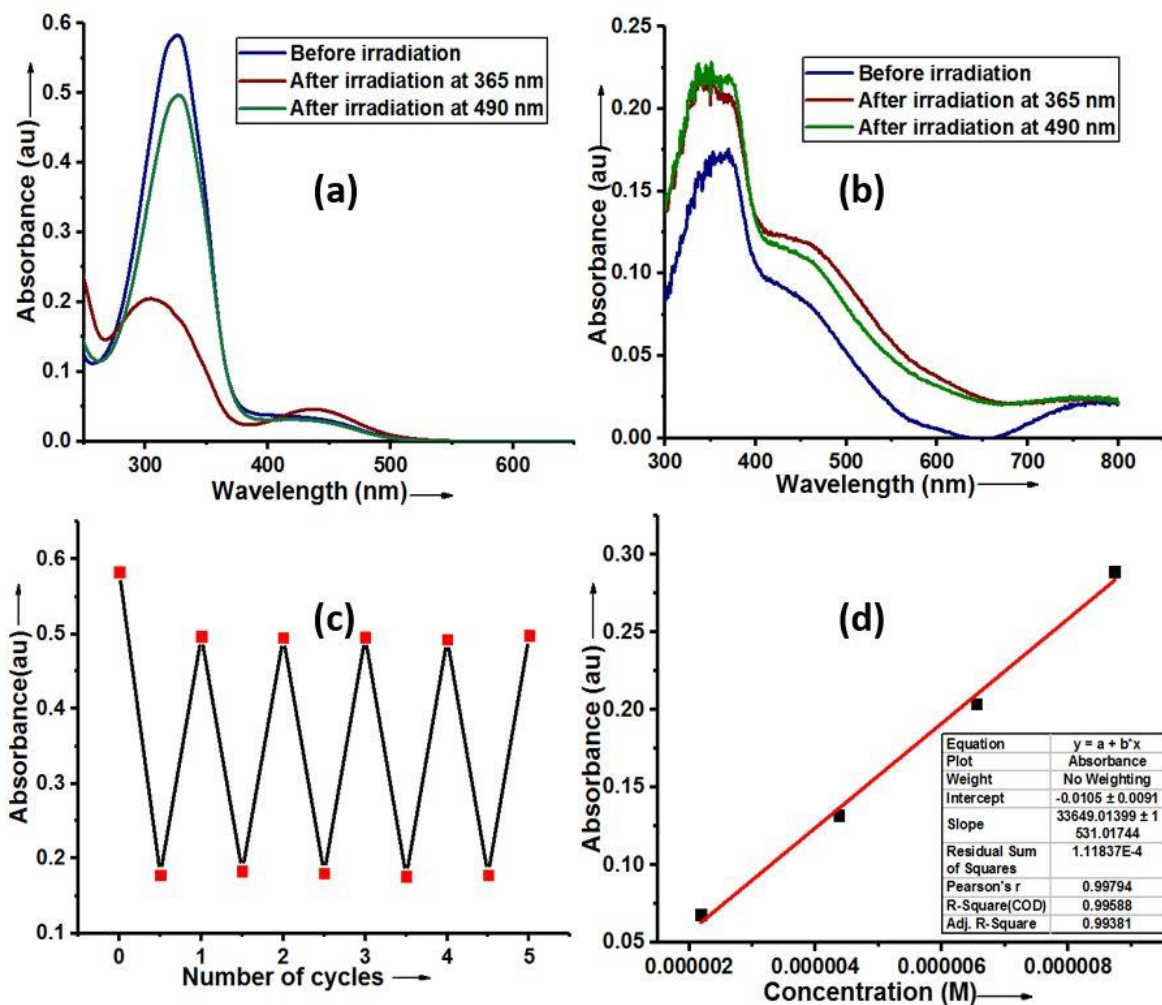
Figure S4-13: Photoswitching behaviour of **L2-Cu:** (a) Forward and reverse photoisomerization (CH₃CN, concentration 17.3 µM; (b) Forward and reverse photoisomerization in solid state (1.1mg of **L2-Cu** diluted with 1300 mg KBr); (c) Photoswitching stability test upto five cycles of **L2-Cu** in CH₃CN (forward isomerization step: 365 nm; reverse isomerizarion step: 490 nm). (d) Estimation of molar extinction coefficient (in Acetonitrile) for the π−π* absorption.
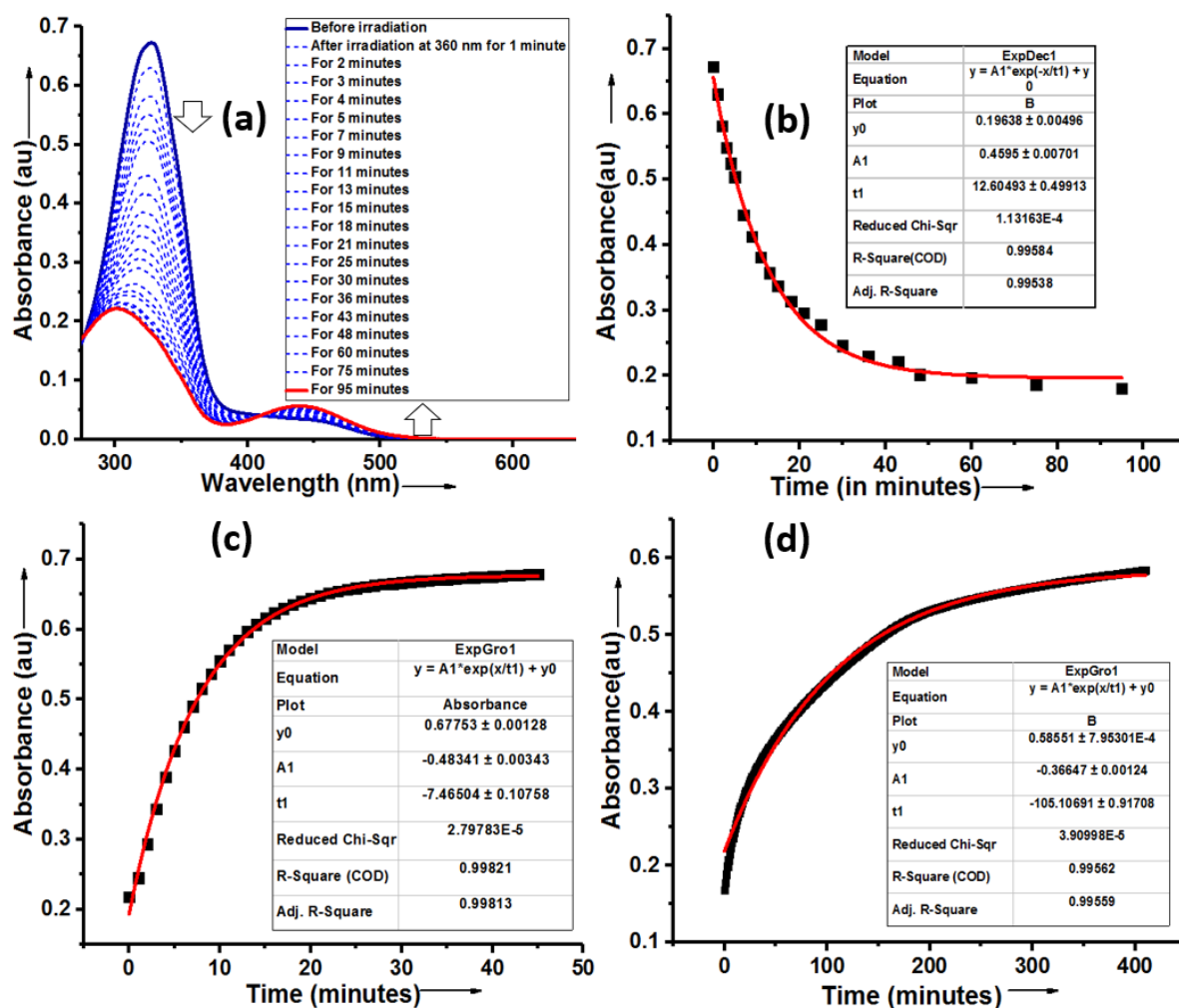
Figure S4-14: Photoswitching and thermal stability aspects of **L2-Cu:** (a) Forward isomerization kinetics measurements of **L2-Cu** under 360 nm (UV-Vis spectroscopic monitoring of approximately 19.9 μM solution in CH_3CN at rt; illumination using 100 μW 360 nm LED); (b) Exponential decay plot for the forward isomerisation step (Absorbance at λ_{max} = 326 nm); (c) First order thermal reverse isomerization kinetics plot and exponential fit of **L2-Cu** (20.1 μM in CH_3CN, 40 °C); (d) First order thermal reverse isomerization kinetics plot and exponential fit of **L2-Cu** (17.4 μM in CH_3CN, 25 °C).

Figure S4-15: Photoswitching behaviour of **L3-Cu:** (a) Forward and reverse photoisomerization (CH₃CN, concentration 25 μM; (b) Forward and reverse photoisomerization in solid state (1.2 mg of **L3-Cu** diluted with 1300 mg KBr); (c) Photoswitching stability test upto five cycles of **L3-Cu** in CH₃CN (forward isomerization step: 365 nm; reverse isomerizarion step: 490 nm). (d) Estimation of molar extinction coefficient (in Acetonitrile) for the π−π* absorption.

Figure S4-16: Photoswitching and thermal stability aspects of **L3-Cu:** (a) Forward isomerization kinetics measurements of **L3-Cu** under 360 nm (UV-Vis spectroscopic monitoring of approximately 28.6 μM solution in CH$_3$CN at rt; illumination using 100 μW 360 nm LED); (b) Exponential decay plot for the forward isomerisation step (Absorbance at λ_{max} = 325 nm); (c) First order thermal reverse isomerization kinetics plot and exponential fit of **L2-Cu** (20.1 μM in CH$_3$CN, 40 °C).

Table S4-1. Experimental and computed data of absorption spectroscopic and photoswitching characteristics of the target compounds

S. No.	Compound	Electronic spectral data (experimental) [a]				Electronic spectral data (calculated) [b]			
		Before switching		After photoswitching		Before switching		After photoswitching	
		$\lambda_{max}/$ $\pi-\pi*$ (ε)	$\lambda_{max}/$ n-$\pi*$	$\lambda_{max}/$ $\pi-\pi*$	$\lambda_{max}/$ n-$\pi*$	$\lambda_{max}/$ $\pi-\pi*$	$\lambda_{max}/$ n-$\pi*$	$\lambda_{max}/$ $\pi-\pi*$	$\lambda_{max}/$ n-$\pi*$
1	**L1**	334 (**35,265 ± 1461**)	421	296	440	332 (1.077) 377 (0.484)	463 (0.053)	291 (0.168) 324 (0.059)	455 (0.106)
2	**L2**	334 (**43237 ± 1641**)	d	295	440	322 (1.711) 374 (0.083)	534 (0.031)	270 (0.101) 294 (0.138)	457 (0.125)
3	**L3**	334 (**34828 ± 586**)	420	296	439	322 (1.625)	480 (0.033)	270 (0.101) 292 (0.033)	460 (0.094)
4	**L1-Cu**	327[c]	416	303	438	325 (0.807) 377 (0.268)	475 (0.093)	294 (0.118)	454 (0.072)
5	**L2-Co**	326 (**31806 ± 1165**)	422	290	436	312 (0.880)	461 (0.028)	328 (0.003)	459 (0.057)
6	**L2-Ni**	326 (**46756 ± 749**)	420	288	436	322 (0.80)	364 (0.128)	292 (0.134)	457 (0.032)
7	**L2-Cu**	326 (**33649 ± 1531**)	d	304	435	339 (0.350)	464 (0.001)	305 (0.080)	456 (0.112)
8	**L3-Cu**	325 (**24432 ± 257**)	411	299	435	321 (0.732)	465 (0.045)	294 (0.117)	460 (0.091)

[a]All the UV-Vis spectroscopic studies have been recorded in CH$_3$CN as a solvent; For all the forward isomerization step 365 nm LED was used; The following wavelengths of light have been used for the reverse isomerization: 470 (**L2**), 490 (**L1, L3, L1-Cu, L2-Co, L2-Ni L2-Cu,** and **L3-Cu**); 2-3 mM concentration solution in CH$_3$CN were taken for all samples; [b]Calculated at TD-DFT level of theory using PCM solvation model with acetonitrile as the solvent; [c]Due to solubility issues, exact concentration is unknown. [d]Exact position is not known because of the broadness of the band.

Table S4-2: PSS data in the forward and reverse photoisomerization in **L1** and the metal complexes in solid state in KBr medium.

S. No.	Compound	PSS composition in solid state photoswitching	
		Forward *EE-ZZ* isomerisation (in terms of %*EE*)	Reverse *ZZ-EE* isomerisation (in terms of %*EE*)
1	**L1**	82	63
4	**L1-Cu**	31	92
5	**L2-Co**	46	81
6	**L2-Ni**	42	81
7	**L2-Cu**	31	92
8	**L3-Cu**	37	84

The following λ_{max} (corresponding to n-π* transition) has been used for estimation of PSS composition in the individual compounds using the formula given below.[6,7]

[**L1** (421 nm), **L1-Cu** (416 nm), **L2-Co** (422 nm), **L2-Ni** (420 nm), **L2-Cu** (460 nm), **L3-Cu** (411 nm)]

% conversion of *EE* isomers(solid state)
$$= \left(1 - \frac{A_{n-\pi*} \text{ absorption before irradiation}}{A_{n-\pi*} \text{ absorption after irradiation at 365 nm}}\right) \text{x}100$$

% conversion of *ZZ* isomers(solid state) $= \dfrac{A_{n-\pi*}\text{absorption after irradiation at 490 nm}}{A_{n-\pi*} \text{ absorption after irradiation at 365 nm}}\text{x } 100$

Table S4-3: PSS data in the forward and reverse photoisomerization in **L1** and the metal complexes in solution phase (in acetonitrile)

S. No.	Compound	PSS composition (%*EE*)[a]		
		Forward	Reverse	Conc. [μM]
1	**L1**	93	92	18
2	**L2**	92	91	16
3	**L3**	95	93	27
4	**L1-Cu**	71	69	x[b]
5	**L2-Co**	83	79	24
6	**L2-Ni**	88	85	12
7	**L2-Cu**	69	64	17.3
8	**L3-Cu**	74	67	25

[a] The PSS compositions have been estimated using the literature procedure. [b] Exact concentration could not be determined because the compound is not completely soluble in CH_3CN.

The λmax (corresponding to $\pi-\pi^*$ transition) has been used for estimation of PSS composition. For all the forward isomerization step 365 nm LED was used; The following wavelengths of light have been used for the reverse photoisomerization: 470 (**L2**), 490 (**L1**, **L3**, **L1-Cu**, **L2-Co**, **L2-Ni**, **L2-Cu**, and **L3-Cu**). The PSS composition has been estimated in the individual compounds using the formula given below.

$$\% \text{ conversion of } EE \text{ isomers} = \left(1 - \frac{A_{\pi-\pi*}\text{absorption after irradiation at 365 nm}}{A_{\pi-\pi*} \text{ absorption before irradiation}}\right) \text{x } 100$$

$$\% \text{ conversion of } ZZ \text{ isomers(solution state)}$$
$$= \left(1 - \frac{A_{\pi-\pi*}\text{absorption after irradiation at 365 nm}}{A_{\pi-\pi*} \text{ absorption after irradiation at 490 nm}}\right) \text{x } 100$$

S5. Analysis of TDDFT results-

TDDFT was performed using PCM solvation model with acetonitrile as the solvent. Various excited states, oscillator strength (f; associated with that particular electronic transition) and electronic transition energy (E) were calculated at B3LYP functional with SDD basis set for metals and SVP basis set for rest of the atoms.

Table S5.1 TD-DFT data of **L1**

Compound	Configuration	λ_{calcd} (nm)	E (eV)	f	Character	Transition
L1	*EE*	463	2.678	0.053	n → π*	HOMO-2(α)→LUMO(α) (20%)
						HOMO-2(α)→LUMO+1(α) (20%)
						HOMO-2(β)→LUMO (β) (20%)
						HOMO-2(β)→LUMO+1(β) (20%)
		377	3.286	0.484	π → π*	HOMO(α)→LUMO(α) (10%)
						HOMO(β)→LUMO(β) (10%)
		332	3.740	1.077	π → π*	HOMO-1(α)→LUMO+1(α) (16%)
						HOMO-1(β)→LUMO+1(β) (16%)
	ZZ	455	2.712	0.106	n → π*	HOMO-1(α)→LUMO(α) (40%)
						HOMO-1(β)→LUMO(β) (40%)
		324	3.819	0.059	π → π*	HOMO-3(α)→LUMO(α) (17%)
						HOMO-3(β)→LUMO(β) (17%)
		291	4.261	0.168	π → π*	HOMO-7(α)→LUMO+1(α) (35%)
						HOMO-7(β)→LUMO+1(β) (35%)

Table S5.2 TD-DFT data depicting the orbitals corresponding to the π−π* and n−π* transitions of **L1** in *EE*-isomeric state
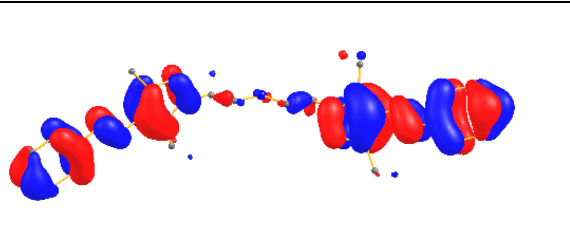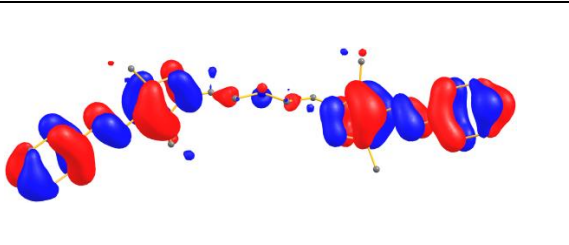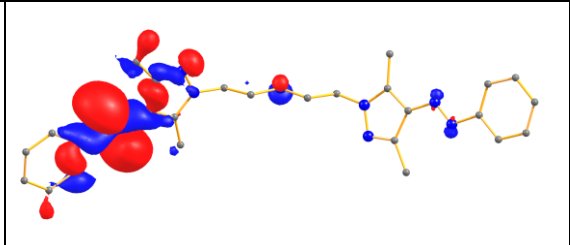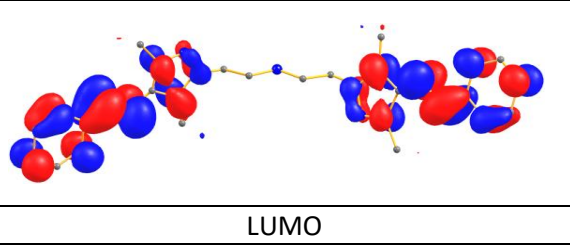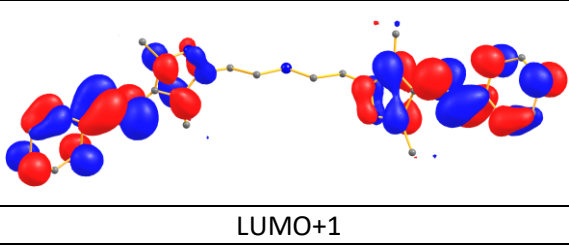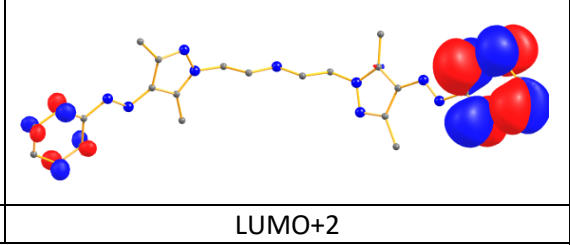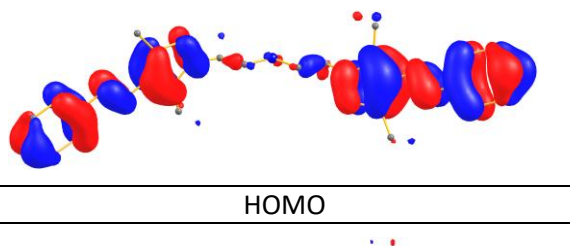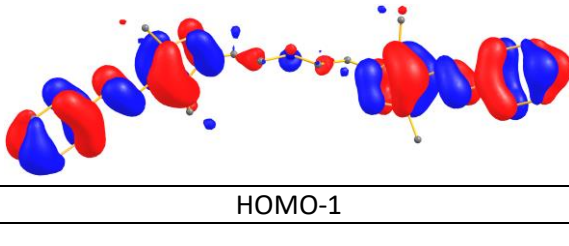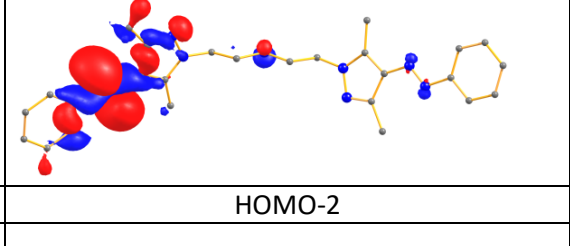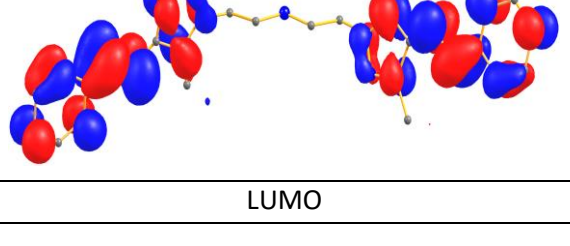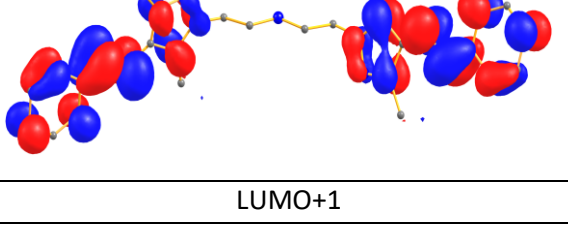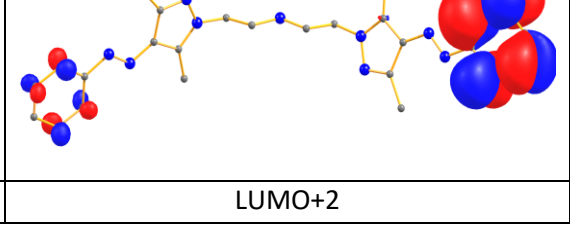
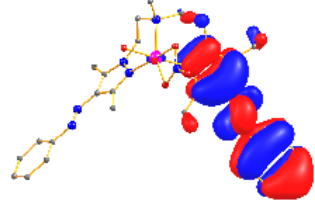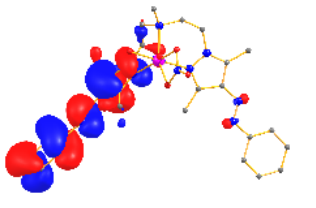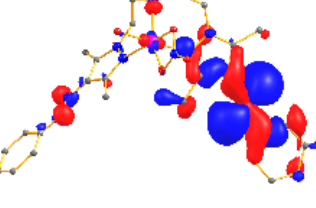| **L1**-*EE* α-spin		
HOMO	HOMO-1	HOMO-2
LUMO	LUMO+1	LUMO+2
β-spin		
HOMO	HOMO-1	HOMO-2
LUMO	LUMO+1	LUMO+2

Table S5.3 TD-DFT data depicting the orbitals corresponding to the π−π* and n−π* transitions of **L1** in *ZZ*-isomeric state

L1-*ZZ* α-spin		
HOMO	HOMO-1	HOMO-2
LUMO	LUMO+1	LUMO+2
β-spin		
HOMO	HOMO-1	HOMO-2
LUMO	LUMO+1	LUMO+2

Table S5.4 TD-DFT data of **L2**

Compound	Configuration	λ_{calcd} (nm)	E(eV)	f	Character	Transition
L2	*EE*	534	2.323	0.031	n → π*	HOMO(α)→LUMO(α) (25%) HOMO(α)→LUMO+1(α) (20%) HOMO(β)→LUMO (β) (25%) HOMO(β)→LUMO+1(β) (20%)
		374	3.16	0.083	π → π*	HOMO-1(α)→LUMO(α) (35%) HOMO-1(β)→LUMO(β) (35%)
		322	3.851	1.711	π → π*	HOMO-2(α)→LUMO+1(α) (27%) HOMO-2(β)→LUMO+1(β) (27%)
	ZZ	457	2.715	0.125	n → π*	HOMO-1(α)→LUMO(α) (38%) HOMO-1(β)→LUMO(β) (38%)
		294	4.221	0.138	π → π*	HOMO-9(α)→LUMO(α) (32%) HOMO-9(β)→LUMO(β) (32%)
		270	4.599	0.101	π → π*	HOMO-1(α)→LUMO+2(α) (24%) HOMO-1(β)→LUMO+2(β) (24%)

Table S5.5 TD-DFT data depicting the orbitals corresponding to the $\pi-\pi^*$ and n$-\pi^*$ transitions of **L2** in *EE*-isomeric state
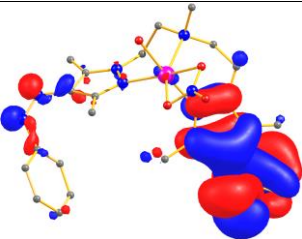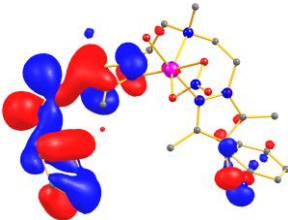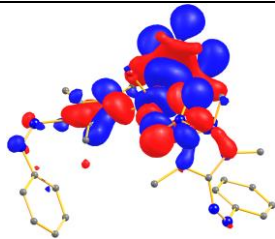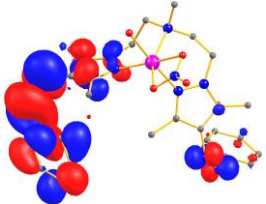
L2-*EE* α-spin		
HOMO	HOMO-1	HOMO-2
LUMO	LUMO+1	LUMO+2
β-spin		
HOMO	HOMO-1	HOMO-2
LUMO	LUMO+1	LUMO+2

Table S5.6 TD-DFT data depicting the orbitals corresponding to the $\pi-\pi^*$ and n$-\pi^*$ transitions of **L2** in *ZZ*-isomeric state
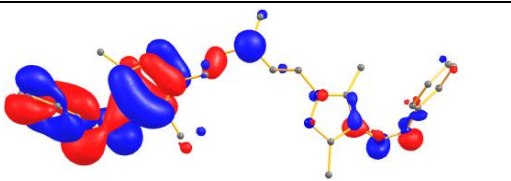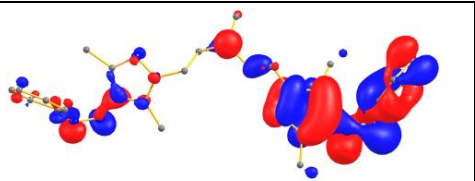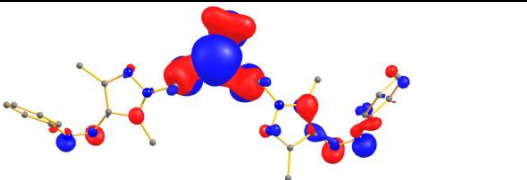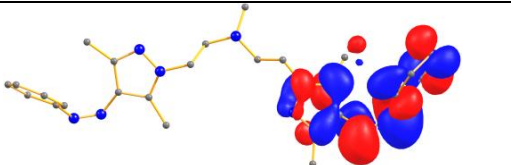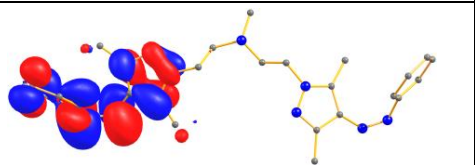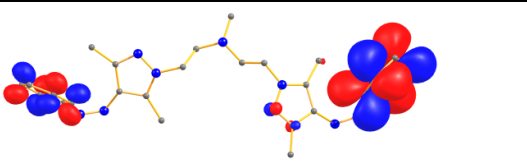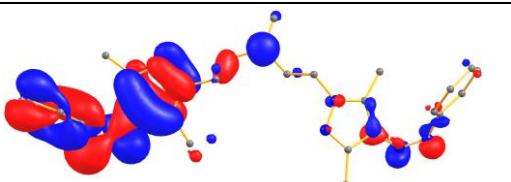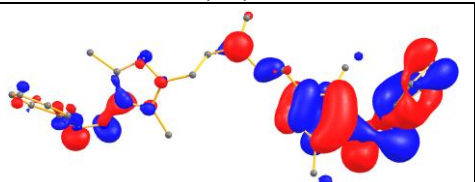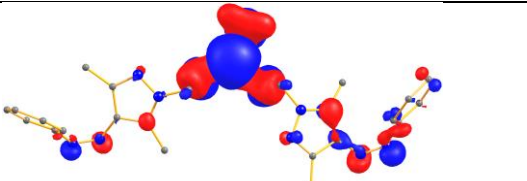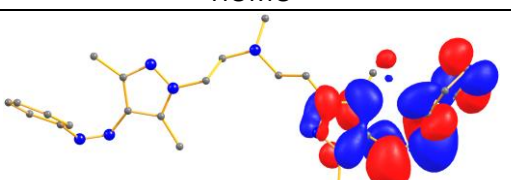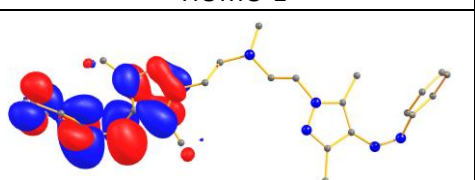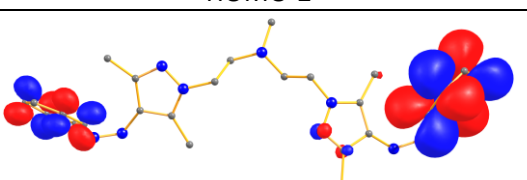
L2-*ZZ* α-spin		
HOMO	HOMO-1	HOMO-2
LUMO	LUMO+1	LUMO+2
β-spin		
HOMO	HOMO-1	HOMO-2
LUMO	LUMO+1	LUMO+2

Table S5.7 TD-DFT data of **L3**
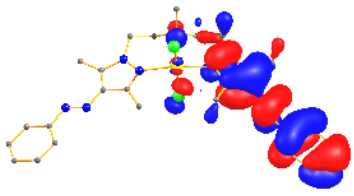
Compound	Configuration	λ_{calcd} (nm)	E(eV)	f	Character	Transition
L3	*EE*	480	2.586	0.033	n → π*	HOMO-1(α)→LUMO(α) (18%) HOMO-1(α)→LUMO+1(α) (15%) HOMO-1(β)→LUMO (β) (18%) HOMO-1(β)→LUMO+1(β) (15%)
		322	3.849	1.625	π → π*	HOMO-2(α)→LUMO(α) (14%) HOMO-2(β)→LUMO(β) (14%)
	ZZ	460	2.697	0.094	n → π*	HOMO-1(α)→LUMO(α) (12%) HOMO-1(β)→LUMO(β) (12%)
		292	4.254	0.033	π → π*	HOMO-8(α)→LUMO(α) (22%) HOMO-8(β)→LUMO(β) (22%)
		270	4.599	0.101	π → π*	HOMO-1(α)→LUMO+2(α) (24%) HOMO-1(β)→LUMO+2(β) (24%)

Table S5.8 TD-DFT data depicting the orbitals corresponding to the π−π* and n−π* transitions of **L3** in *EE*-isomeric state
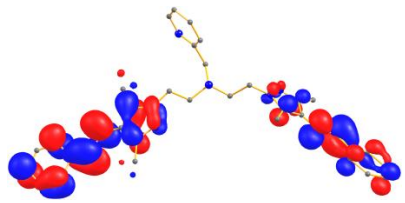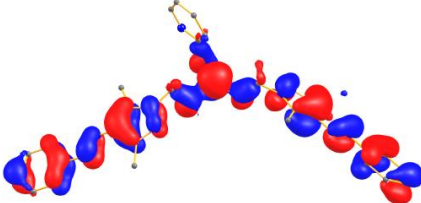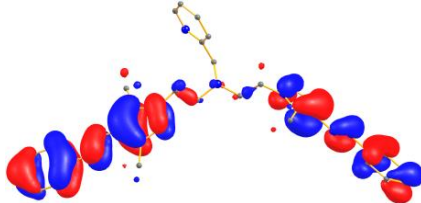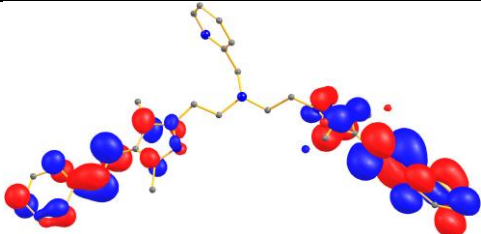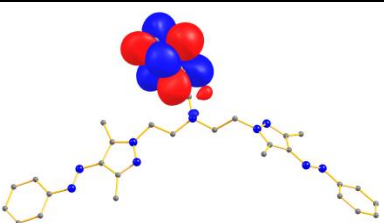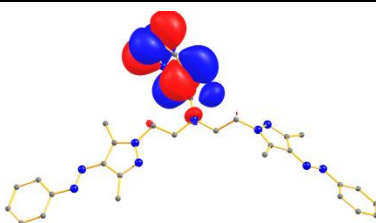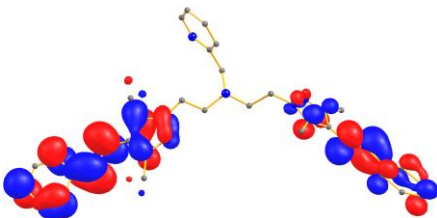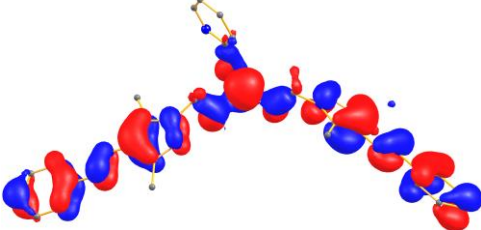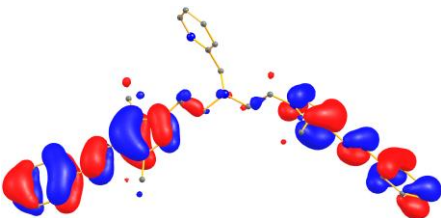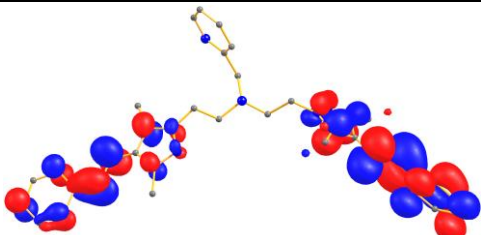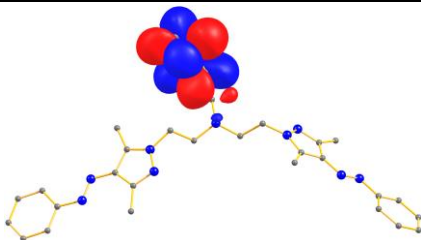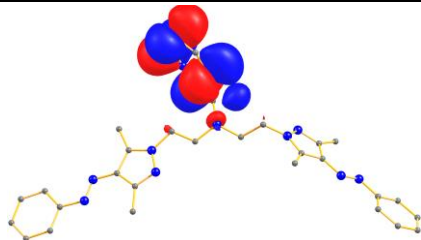
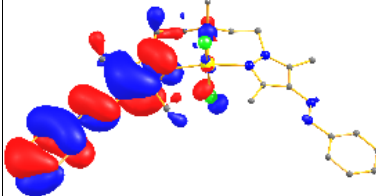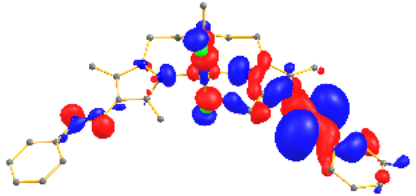| L3-EE α-spin		
HOMO	HOMO-1	HOMO-2
LUMO	LUMO+1	LUMO+2
β-spin		
HOMO	HOMO-1	HOMO-2
LUMO	LUMO+1	LUMO+2

Table S5.9 TD-DFT data depicting the orbitals corresponding to the π−π* and n−π* transitions of **L3** in *ZZ*-isomeric state
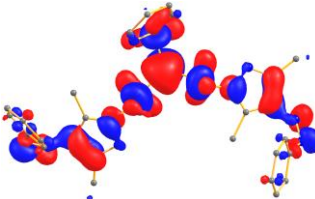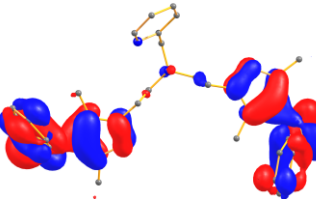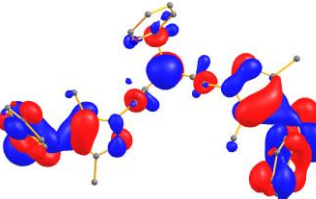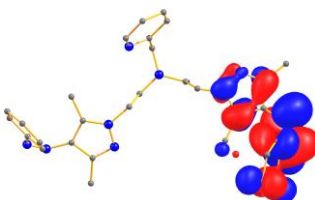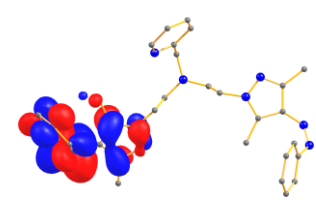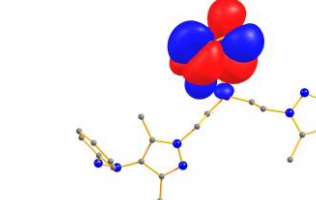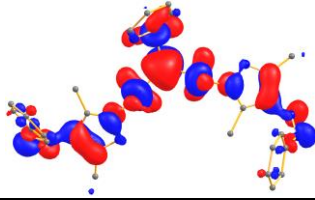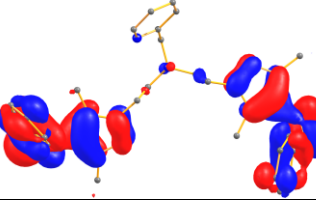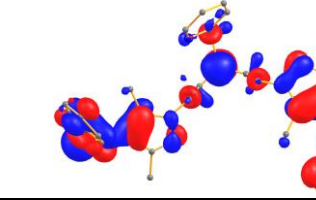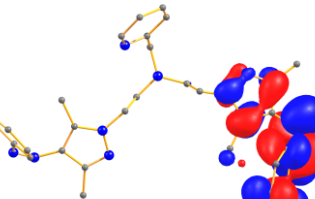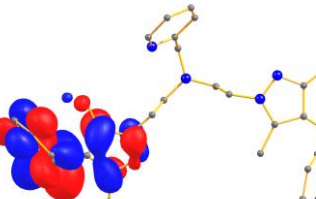
L3-ZZ α-spin		
HOMO	HOMO-1	HOMO-2
LUMO	LUMO+1	LUMO+2
β-spin		
HOMO	HOMO-1	HOMO-2
LUMO	LUMO+1	LUMO+2

Table S5.10 TD-DFT data of **L1-Cu**

Compound	Configuration	λ_{calcd} (nm)	E(eV)	f	Character	Transition
L1-Cu	*EE*	475	2.608	0.093	n → π*	HOMO-2(α)→LUMO(α) (70%)
		377	3.286	0.268	π → π*	HOMO-3(α)→LUMO+1(α) (50%)
		325	3.808	0.807	π → π*	HOMO(α)→LUMO+1(α) (12%)
	ZZ	454	2.728	0.072	n → π*	HOMO-1(β)→LUMO+3(β) (12%)
		294	4.215	0.118	π → π*	HOMO-5(α)→LUMO+1(α) (11%)

Table S5.11 TD-DFT data depicting the orbitals corresponding to the π−π* and n−π* transitions of **L1-Cu** in *EE*-isomeric state

L1-Cu-*EE* α-spin		
HOMO	HOMO-1	HOMO-2
LUMO	LUMO+1	LUMO+2
β-spin		
HOMO	HOMO-1	HOMO-2
LUMO	LUMO+1	LUMO+2
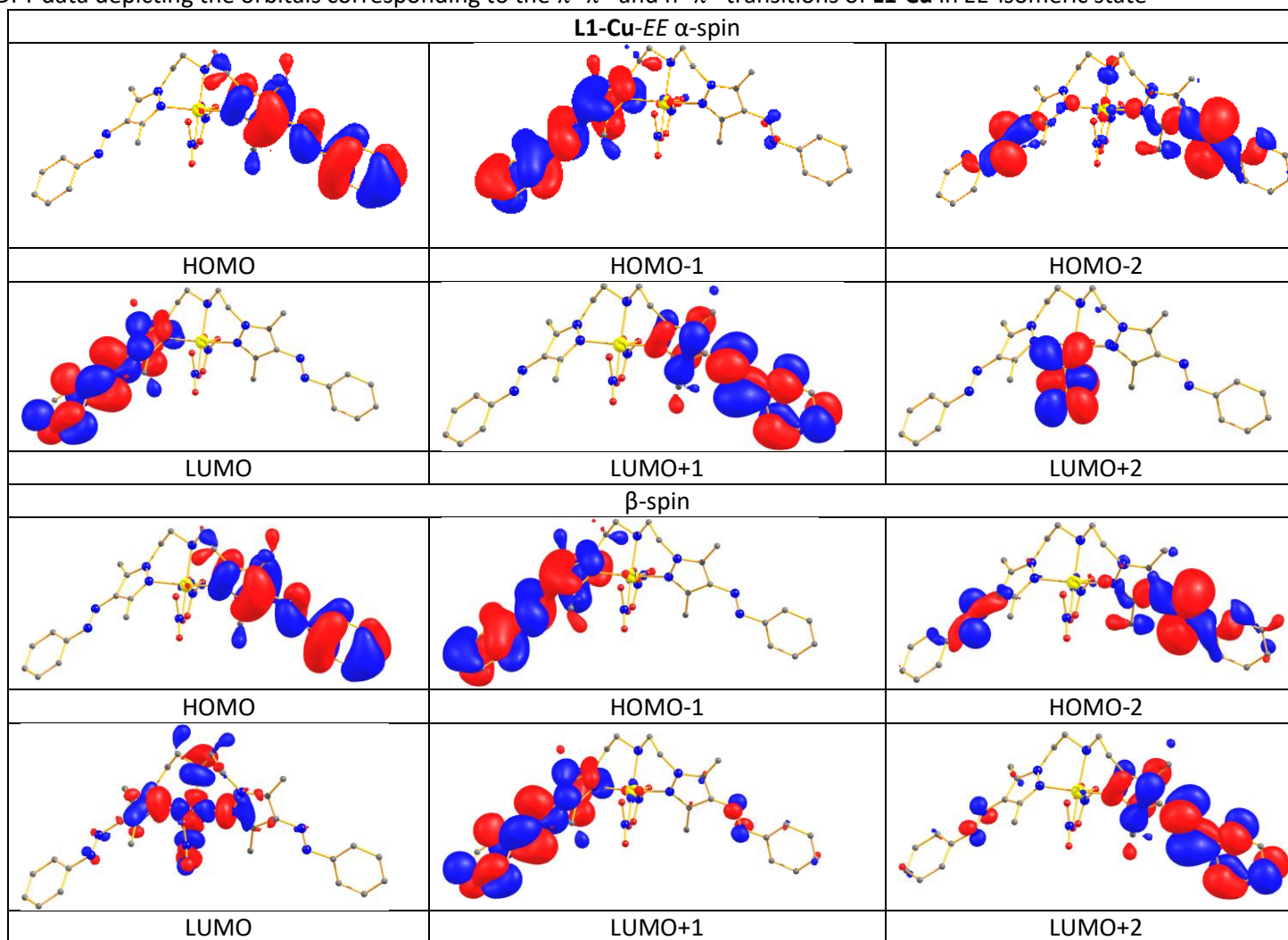
Table S5.12 TD-DFT data depicting the orbitals corresponding to the π−π* and n−π* transitions of **L1-Cu** in *ZZ*-isomeric state
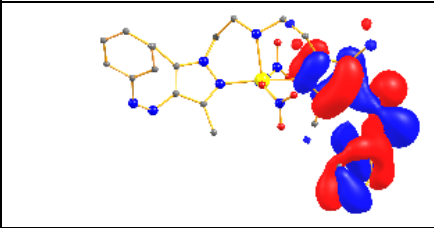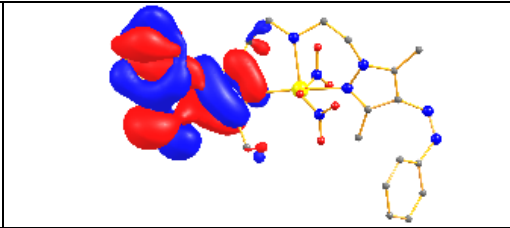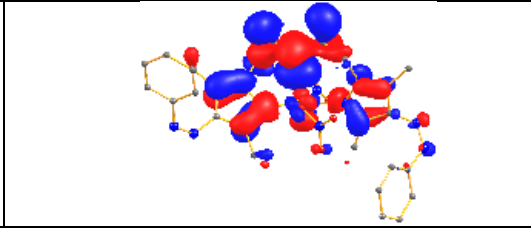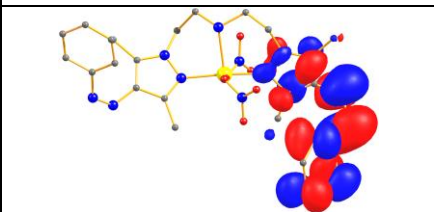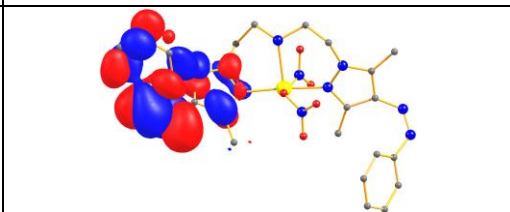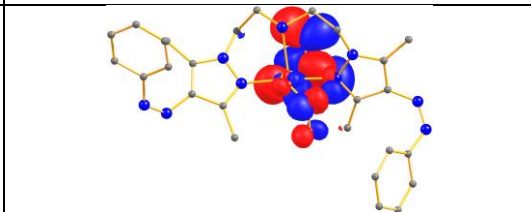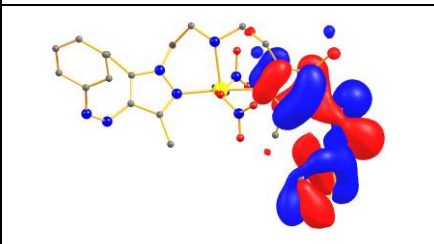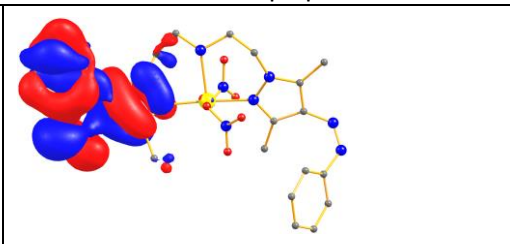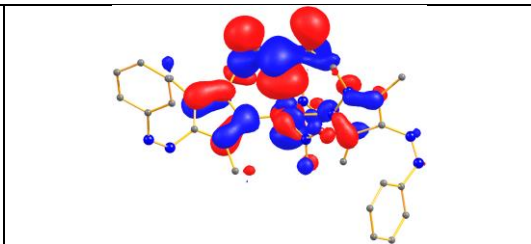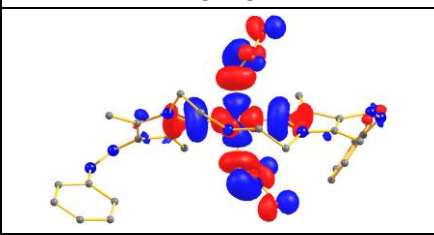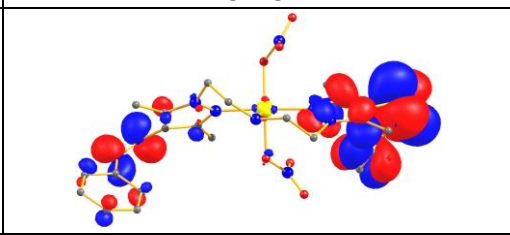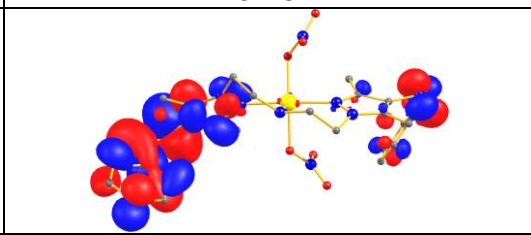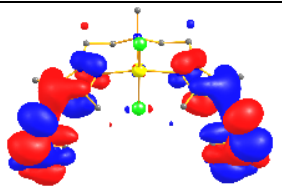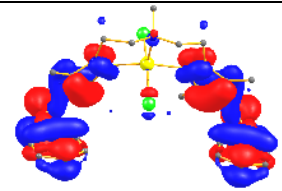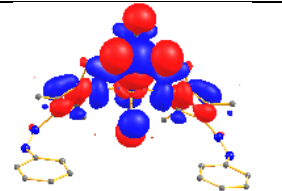
L1-Cu-ZZ α-spin		
HOMO	HOMO-1	HOMO-2
LUMO	LUMO+1	LUMO+2
β-spin		
HOMO	HOMO-1	HOMO-2
LUMO	LUMO+1	LUMO+2

Table S5.13 TD-DFT data of **L2-Co**

Compound	Configuration	λ_{calcd} (nm)	E(eV)	f	Character	Transition
L2-Co	*EE*	461	2.689	0.028	n → π*	HOMO-1(β)→LUMO(β) (80%)
		312	3.975	0.880	π → π*	HOMO-1(α)→LUMO(α) (17%) HOMO-1(β)→LUMO+1(β) (10%)
	ZZ	459	2.701	0.057	n → π*	HOMO-1(α)→LUMO(α) (17%) HOMO-1(β)→LUMO+1(β) (16%)
		328	3.785	0.003	π → π*	HOMO-1(β)→LUMO+1(β) (50%)

Table S5.14 TD-DFT data depicting the orbitals corresponding to the π−π* and n−π* transitions of **L2-Co** in *EE*-isomeric state
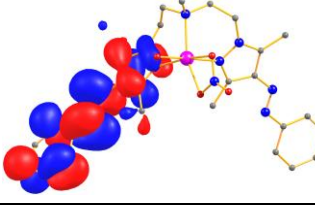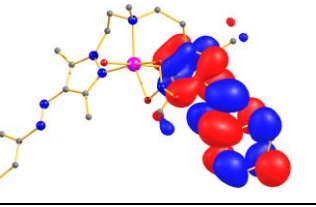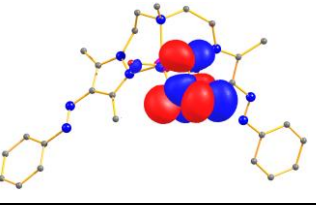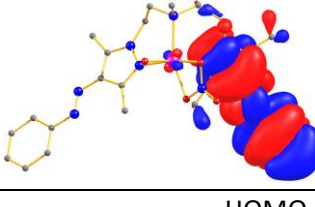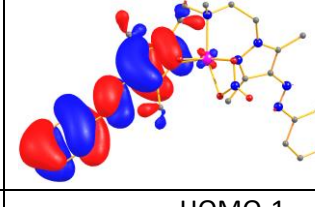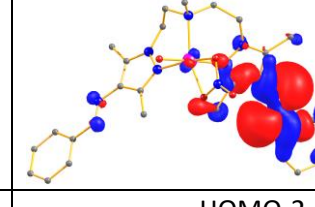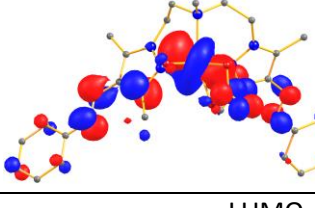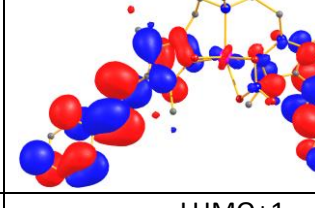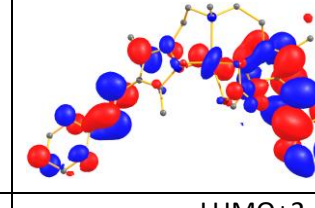
L2 Co-EE α-spin		
HOMO	HOMO-1	HOMO-2
LUMO	LUMO+1	LUMO+2
β-spin		
HOMO	HOMO-1	HOMO-2
LUMO	LUMO+1	LUMO+2

Table S5.15 TD-DFT data depicting the orbitals corresponding to the π−π* and n−π* transitions of **L2-Co** in *ZZ*-isomeric state
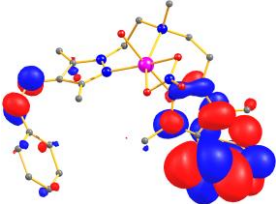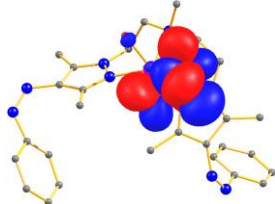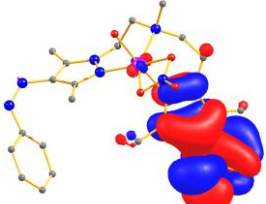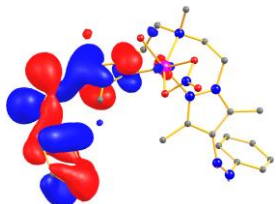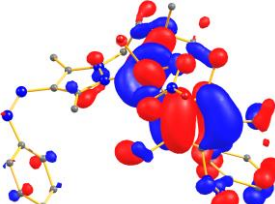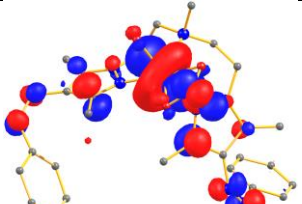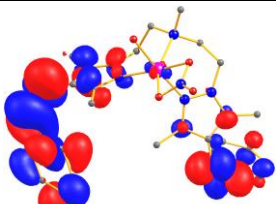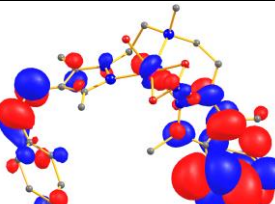
L2 Co-ZZ α-spin		
HOMO	HOMO-1	HOMO-2
LUMO	LUMO+1	LUMO+2
β-spin		
HOMO	HOMO-1	HOMO-2
LUMO	LUMO+1	LUMO+2

Table S5.16 TD-DFT data of **L2-Cu**

Compound	Configuration	λ$_{calcd}$ (nm)	E(eV)	f	Character	Transition
L2-Cu	*EE*	464	2.674	0.001	n → π*	HOMO-3(α)→LUMO(α) (45%) HOMO-2(β)→LUMO+1(β) (34%)
		339	3.659	0.350	π → π*	HOMO-1(α)→LUMO(α) (10%) HOMO-1(β)→LUMO+1(β) (10%)
	ZZ	456	2.717	0.112	n → π*	HOMO(α)→LUMO+1(α) (22%) HOMO(β)→LUMO+2(β) (22%)
		305	4.063	0.080	π → π*	HOMO-5(α)→LUMO(α) (47%)

Table S5.17 TD-DFT data depicting the orbitals corresponding to the π−π* and n−π* transitions of **L2-Cu** in *EE*-isomeric state
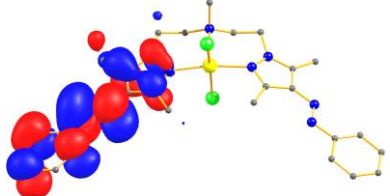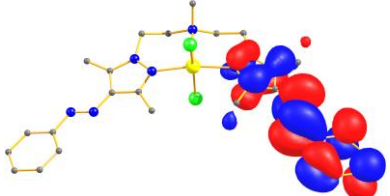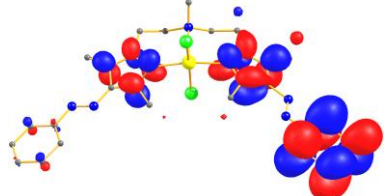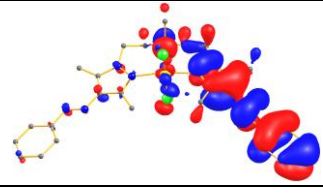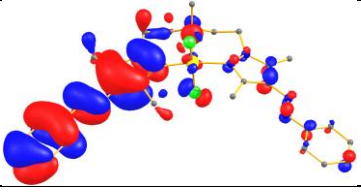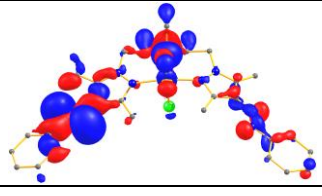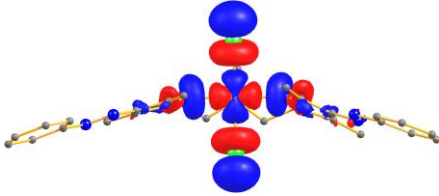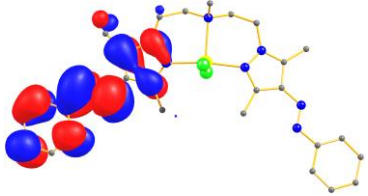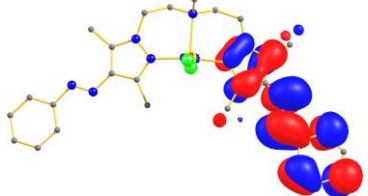
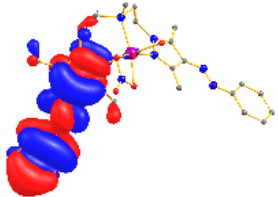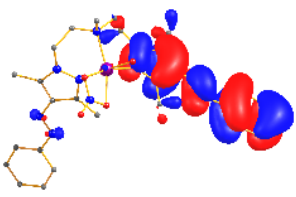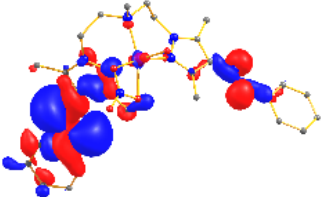| L2 Cu-*EE* α-spin		
HOMO	HOMO-1	HOMO-2
LUMO	LUMO+1	LUMO+2
β-spin		
HOMO	HOMO-1	HOMO-2
LUMO	LUMO+1	LUMO+2

Table S5.18 TD-DFT data depicting the orbitals corresponding to the π−π* and n−π* transitions of **L2-Cu** in *ZZ*-isomeric state
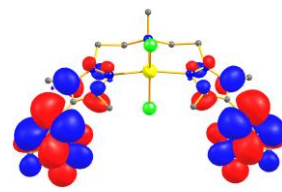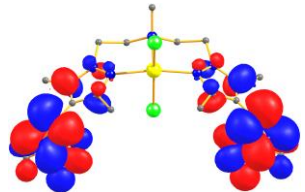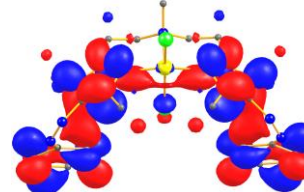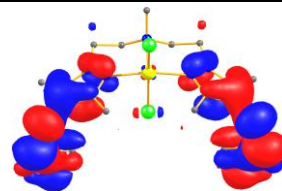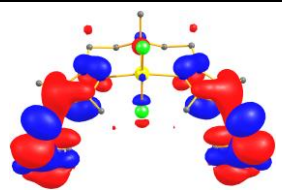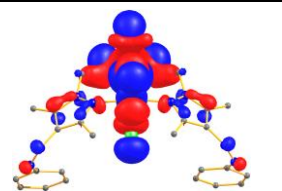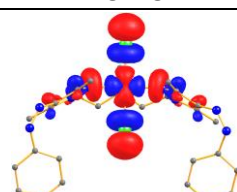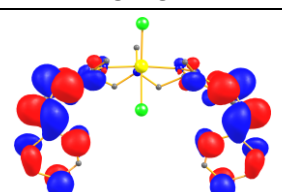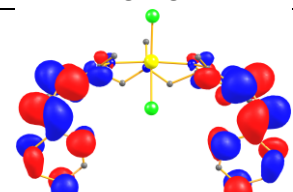
L2 Cu-ZZ α-spin		
HOMO	HOMO-1	HOMO-2
LUMO	LUMO+1	LUMO+2
β-spin		
HOMO	HOMO-1	HOMO-2
LUMO	LUMO+1	LUMO+2

Table S5.19 TD-DFT data of **L2-Ni**

Compound	Configuration	λ_{calcd} (nm)	E(eV)	f	Character	Transition
L2-Ni	*EE*	364	3.411	0.128	n → π*	HOMO-2 (β)→LUMO+1(β) (62%)
		322	3.842	0.80	π → π*	HOMO-1(α)→LUMO(α) (15%)
	ZZ	457	2.713	0.032	n → π*	HOMO-1(α)→LUMO(α) (25%) HOMO-1(β)→LUMO(β) (25%)
		292	4.246	0.134	π → π*	HOMO-8(β)→LUMO+1(β) (16%) HOMO-9(α)→LUMO+1(α) (16%)

Table S5.20 TD-DFT data depicting the orbitals corresponding to the π−π* and n−π* transitions of **L2-Ni** in *EE*-isomeric state
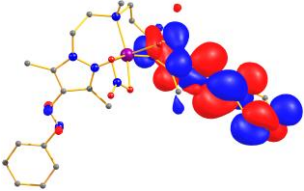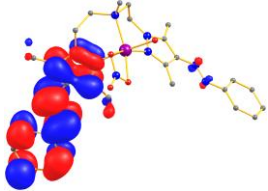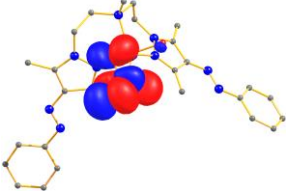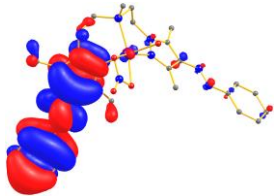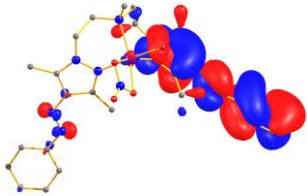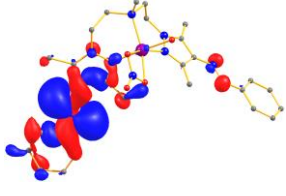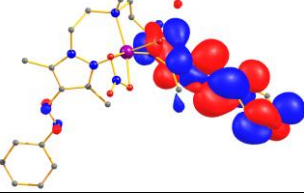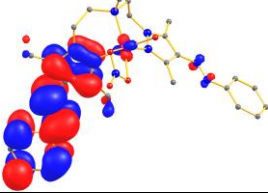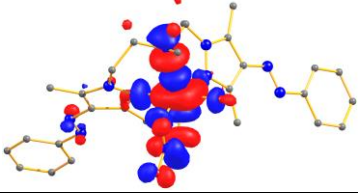
L2 Ni-*EE* α-spin		
HOMO	HOMO-1	HOMO-2
LUMO	LUMO+1	LUMO+2
β-spin		
HOMO	HOMO-1	HOMO-2
LUMO	LUMO+1	LUMO+2

Table S5.21 TD-DFT data depicting the orbitals corresponding to the π–π* and n–π* transitions of **L2-Ni** in *ZZ*-isomeric state

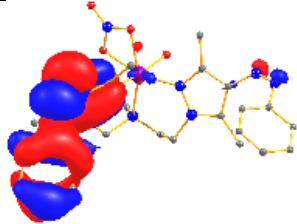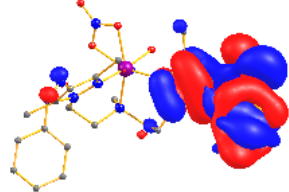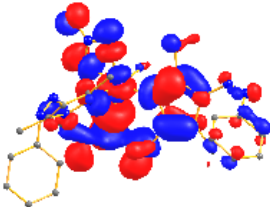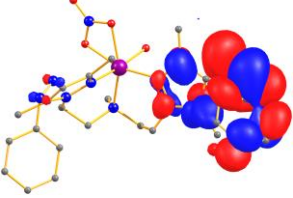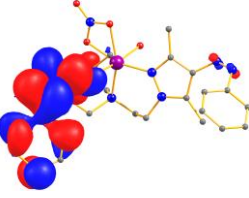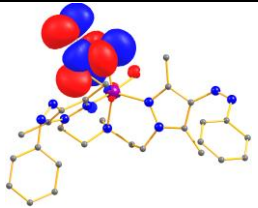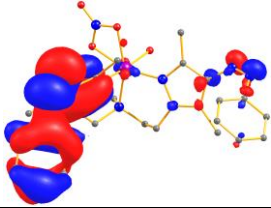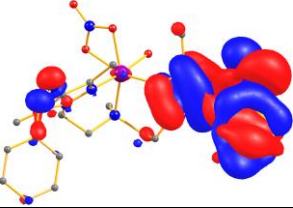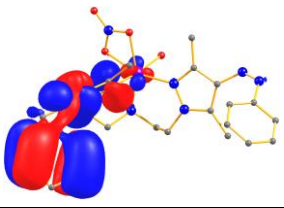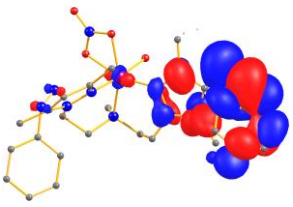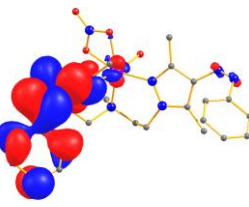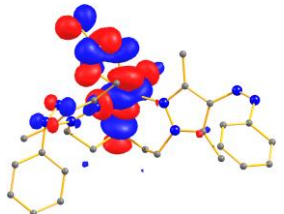| L2 Ni-*ZZ* β-spin		
HOMO	HOMO-1	HOMO-2
LUMO	LUMO+1	LUMO+2
β-spin		
HOMO	HOMO-1	HOMO-2
LUMO	LUMO+1	LUMO+2

Table S5.22 TD-DFT data of **L3-Cu**

Compound	Configuration	λ$_{calcd}$ (nm)	E(eV)	f	Character	Transition
L3-Cu	*EE*	465	2.644	0.045	n → π*	HOMO-2(β)→LUMO+1(β) (90%)
		321	3.862	0.732	π → π*	HOMO(α)→LUMO+1(α) (15%) HOMO(β)→LUMO+2(β) (15%)
	ZZ	460	2.698	0.091	n → π*	HOMO-1(α)→LUMO(α) (25%) HOMO-1(β)→LUMO+1(β) (25%)
		294	4.200	0.117	π → π*	HOMO-10(α)→LUMO+1(α) (12%)

Table S5.23 TD-DFT data depicting the orbitals corresponding to the π−π* and n−π* transitions of **L3-Cu** in *EE*-isomeric state
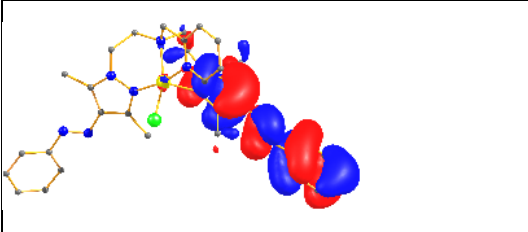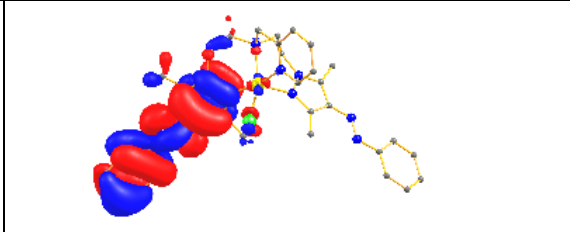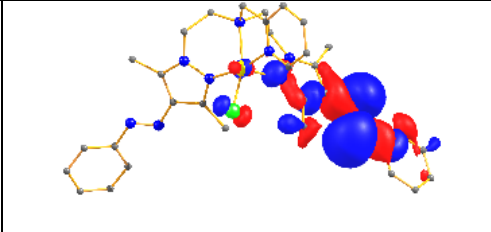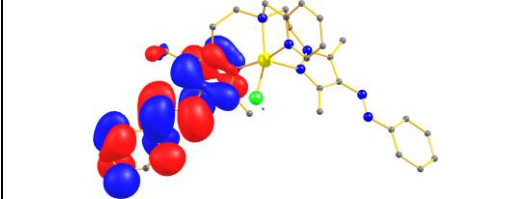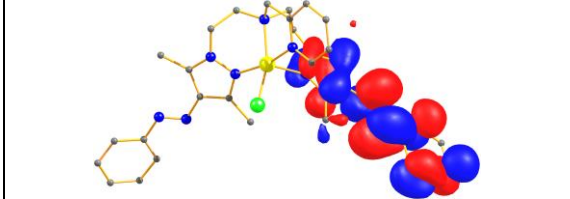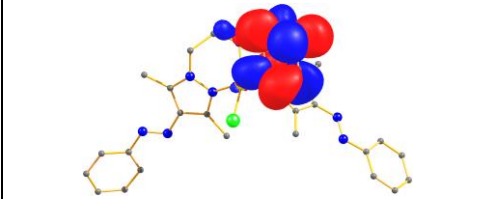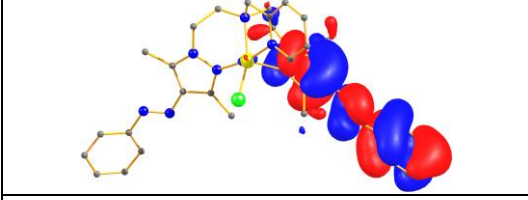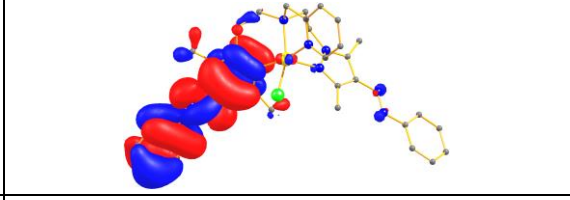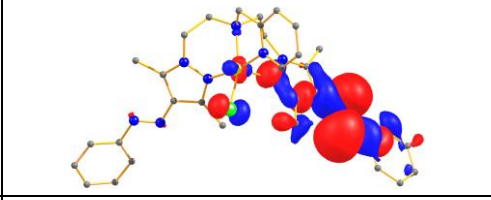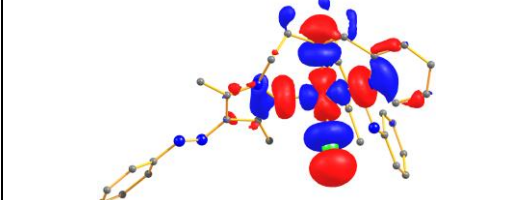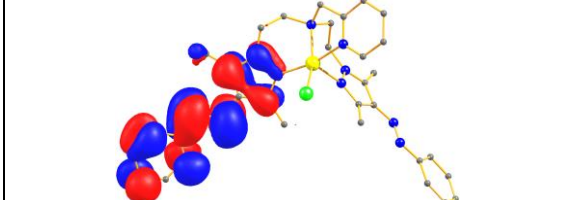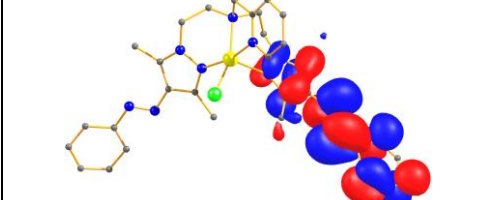
L3 Cu-EE α-spin		
HOMO	HOMO-1	HOMO-2
LUMO	LUMO+1	LUMO+2
β-spin		
HOMO	HOMO-1	HOMO-2
LUMO	LUMO+1	LUMO+2

Table S5.24 TD-DFT data depicting the orbitals corresponding to the π−π* and n−π* transitions of **L3-Cu** in *ZZ*-isomeric state

L3 Cu-ZZ α-spin		
HOMO	HOMO-1	HOMO-2
LUMO	LUMO+1	LUMO+2
β-spin		
HOMO	HOMO-1	HOMO-2
LUMO	LUMO+1	LUMO+2

Figure S5-1: A comparison between experimental and calculated π–π* and n-π* bands of **L1**, **L2** and **L3**
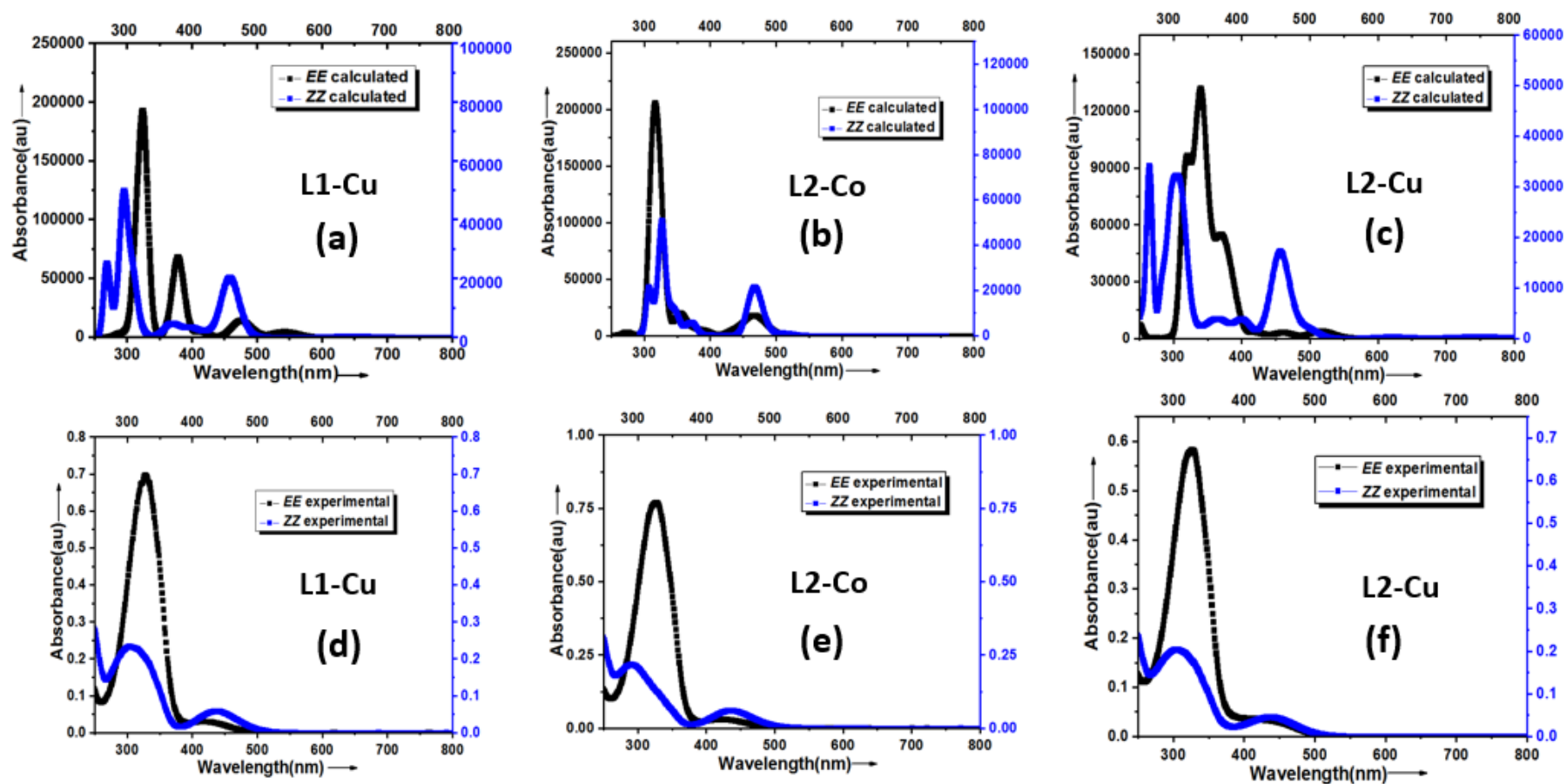
Figure S5-2: A comparison between experimental and calculated $\pi-\pi^*$ and n-π^* bands of **L1-Cu**, **L2-Co and L2-Cu**
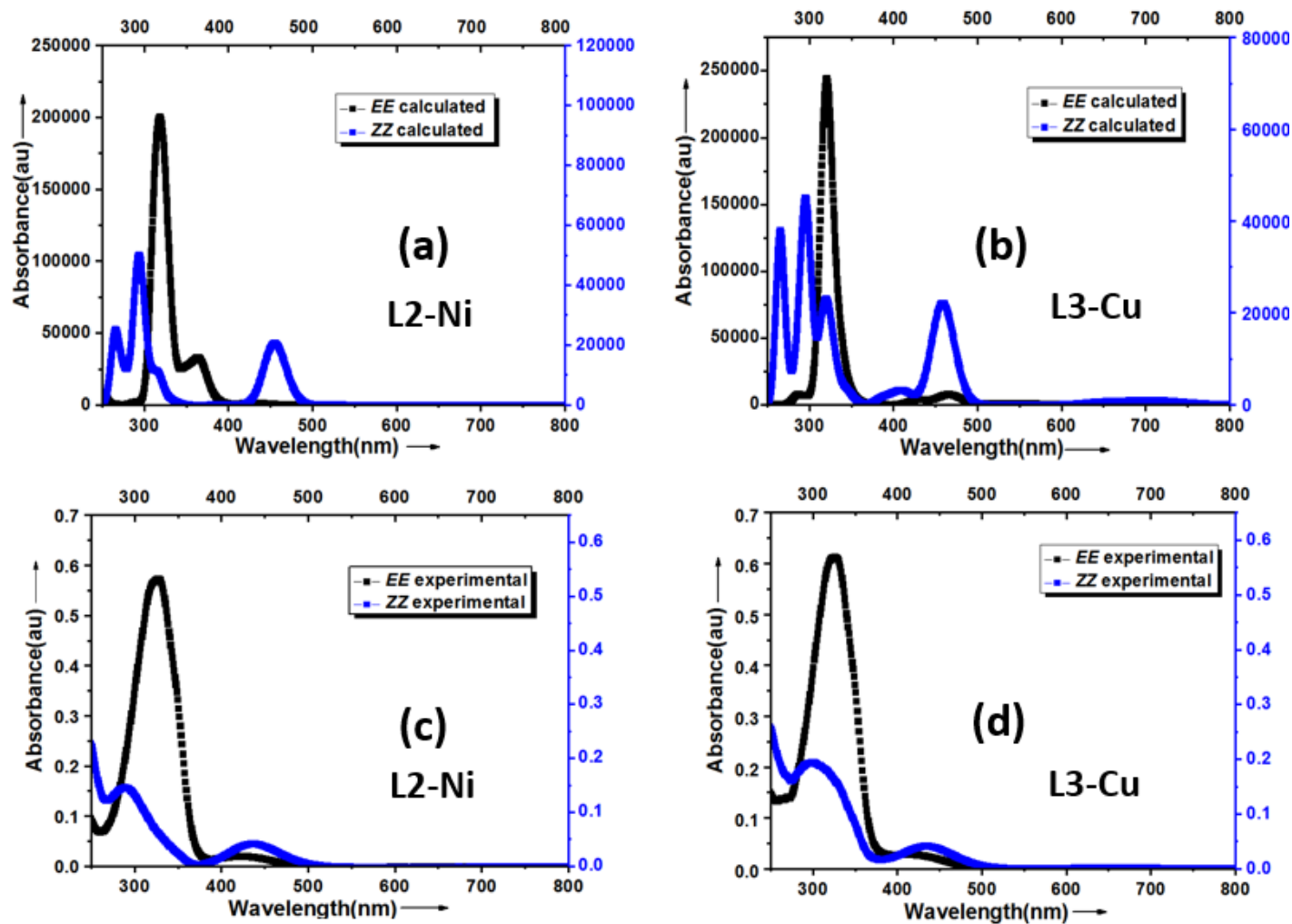
Figure S5-3: A comparison between experimental and calculated π–π* and n-π* bands of **L2-Ni** and **L3-Cu**

S6. Isomerization kinetics data

Table S6-1. Forward Isomerization Kinetics data

(First order formation rate constants for the *ZZ*-isomer obtained from the UV-Vis spectroscopic measurements in CH_3CN at rt, and an exponential decay fit of the resulting data). 100 µW 360 nm LED light has been used for forward isomerisation.

	Compound	Rate constant (min^{-1})[a]	Conc. [µM]
1	**L1**	$1.9X10^{-1} \pm 1.1X10^{-2}$	20.7
2	**L2**	$1.8X10^{-1} \pm 6.7X10^{-3}$	17.9
3	**L3**	$3.0X10^{-1} \pm 3.1X10^{-2}$	19
4	**L1-Cu**	$4.6X10^{-2} \pm 1.1X10^{-3}$	**X**
5	**L2-Co**	$7.1X10^{-2} \pm 1.6X10^{-3}$	20.7
6	**L2-Ni**	$9.0X10^{-2} \pm 8.9X10^{-4}$	14.6
7	**L2-Cu**	$7.9X10^{-2} \pm 3.1X10^{-3}$	19.9
8	**L3-Cu**	$5.2X10^{-2} \pm 6.0X10^{-4}$	28.6

Table S6-2. Thermal reverse isomerization kinetics data:

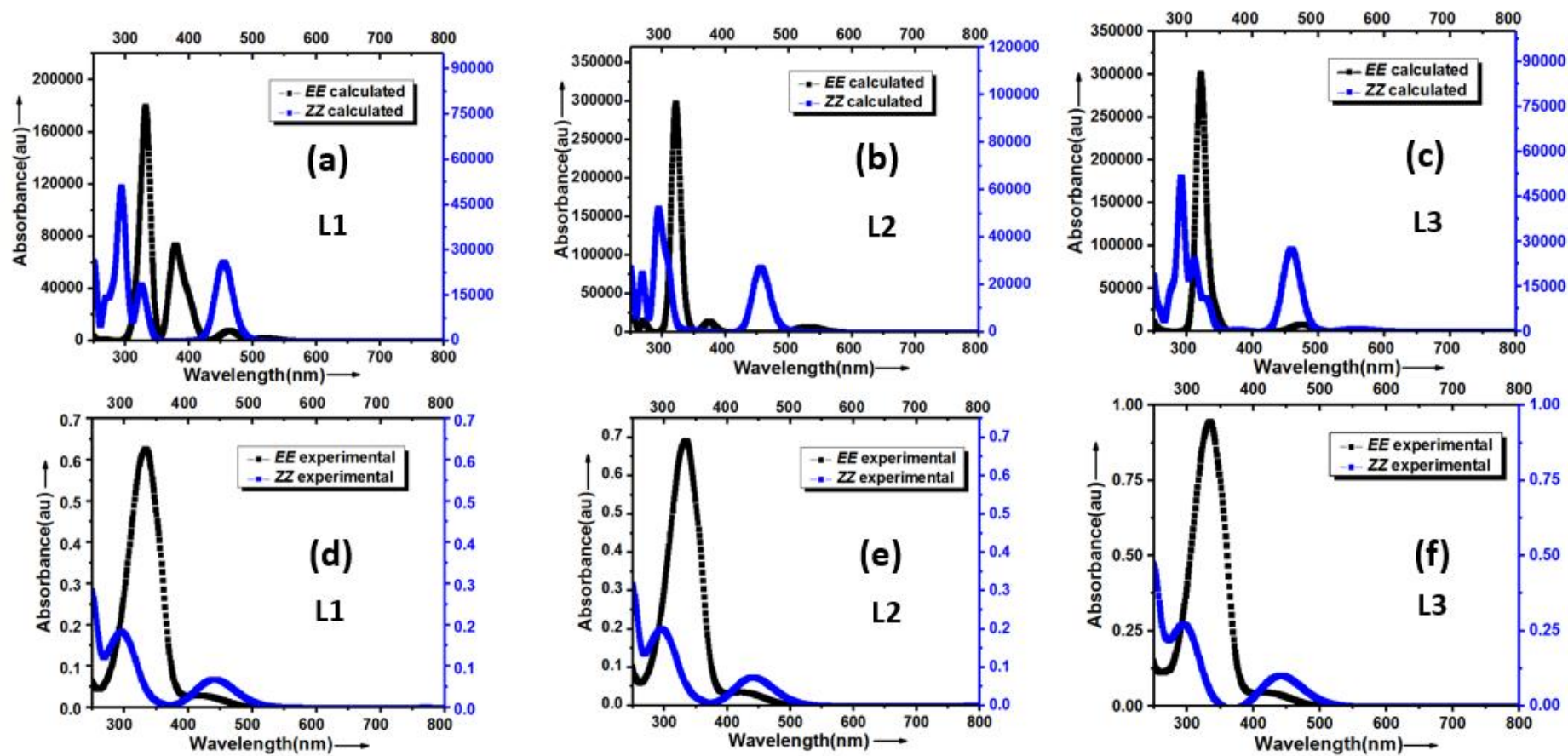|	Compound	Temperature (°C)	Rate constant (min^{-1})[a]	Half life[a] (min)	Conc. [µM]
1	**L1**	40	$3.8X10^{-4} \pm 2.3X10^{-6}$	1832	16
2	**L2**	40	$3.4X10^{-4} \pm 3.8X10^{-6}$	2044	17.8
3	**L3**	40	$3.9X10^{-4} \pm 1.2X10^{-6}$	1770	16
4	**L1-Cu**	25	$2.0X10^{-1} \pm 4.0X10^{-3}$	3	~20*
		40	$6.0X10^{-1} \pm 1.9X10^{-2}$	1	~20*
5	**L2-Co**	25	$3.6X10^{-4} \pm 4.7X10^{-7}$	1929	21.3
		40	$4.0X10^{-2} \pm 3.6X10^{-4}$	24	22.3
6	**L2-Ni**	40	$7.6X10^{-4} \pm 4.2X10^{-6}$	1315	17.5
7	**L2-Cu**	25	$9.5X10^{-3} \pm 8.3X10^{-5}$	73	17.4
		40	$1.3X10^{-1} \pm 1.9X10^{-3}$	5	20.1
8	**L3-Cu**	40	$3.8X10^{-4} \pm 4.4X10^{-6}$	2600	20.1
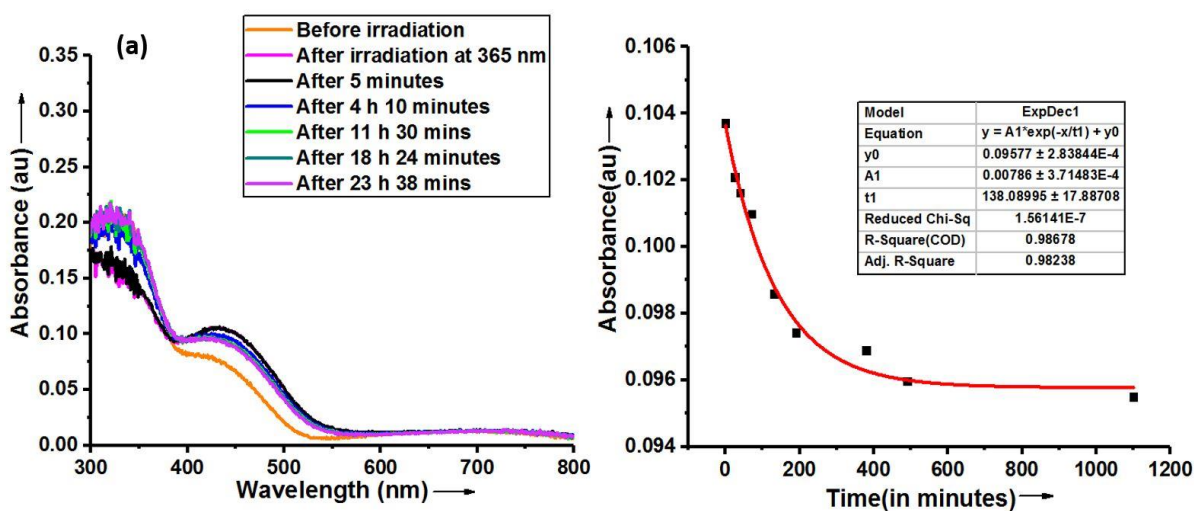
Figure S6-1: Thermal reverse isomerization kinetics of **L1-Cu** in KBr medium (0.9 mg in 1000 mg KBr) at room temperature. (a) Changes in the absorption profiles in the n-π^* region depicting thermal reverse isomerization kinetics; (b) Exponential decay plot for the estimation of first order rate constant (k_{rev}= 7.2 x 10^{-3} ± 9.4 x 10^{-4}) by plotting the changes in the absorption values at 416 nm up to 23h 38 min.

S7. Quantification of photoisomers using ^{1}H NMR spectroscopy

Figure S7-1: Analysis of photoswitching and estimation of PSS composition using ^{1}H-NMR spectroscopic studies of **L1** in d6-DMSO (5 mM) (a) before irradiation; (b) after irradiation at 365 nm; (c) after irradiation at 490 nm. (The normalized integral values corresponding to methyl signal was used for the estimation of PSS composition.)
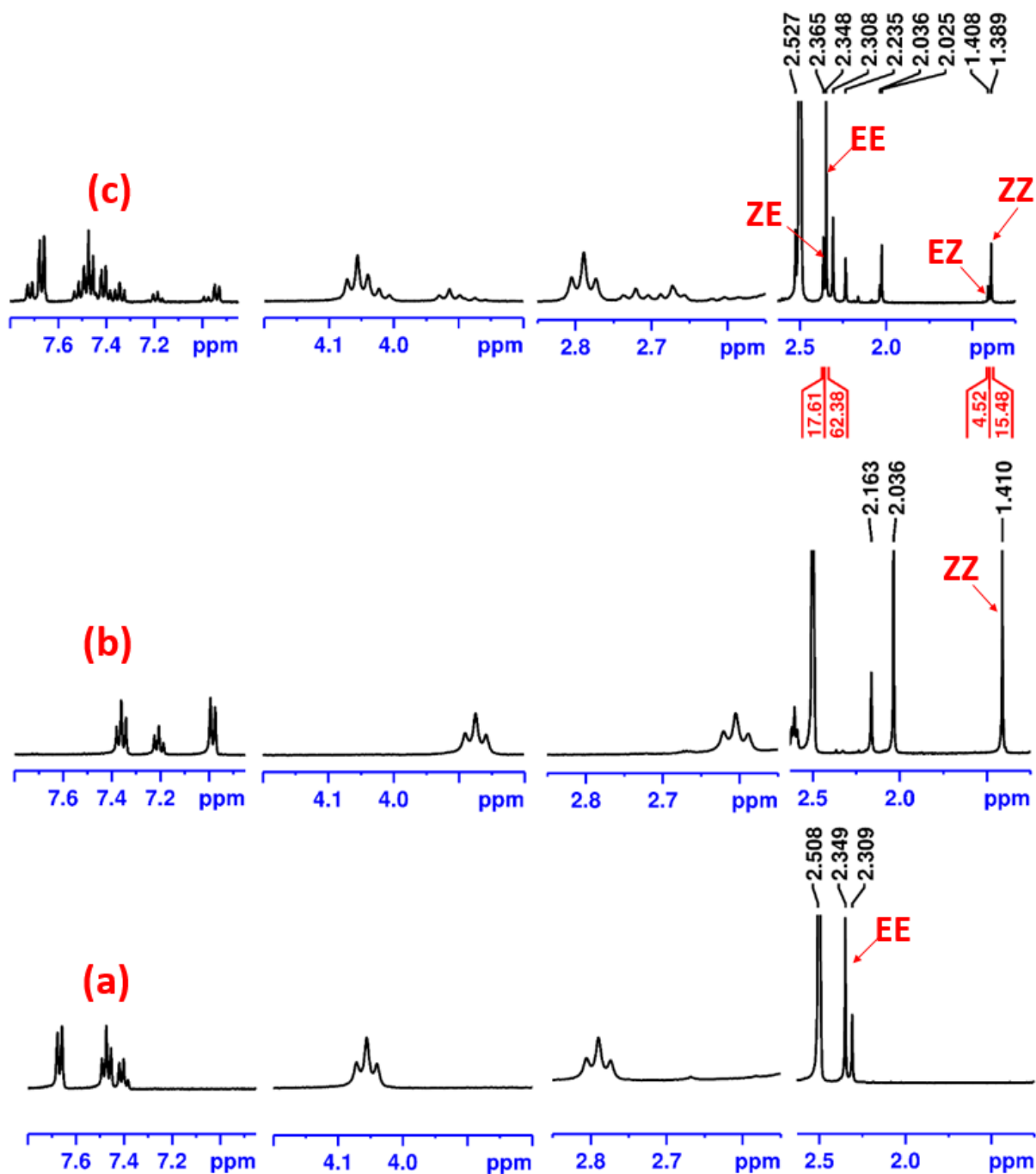
Figure S7-2: Analysis of photoswitching and estimation of PSS composition using ^{1}H-NMR spectroscopic studies of **L2** in d6-DMSO (6 mM) (a) before irradiation; (b) after irradiation at 365 nm; (c) after irradiation at 470 nm. (The normalized integral values corresponding to methyl signal was used for the estimation of PSS composition.)
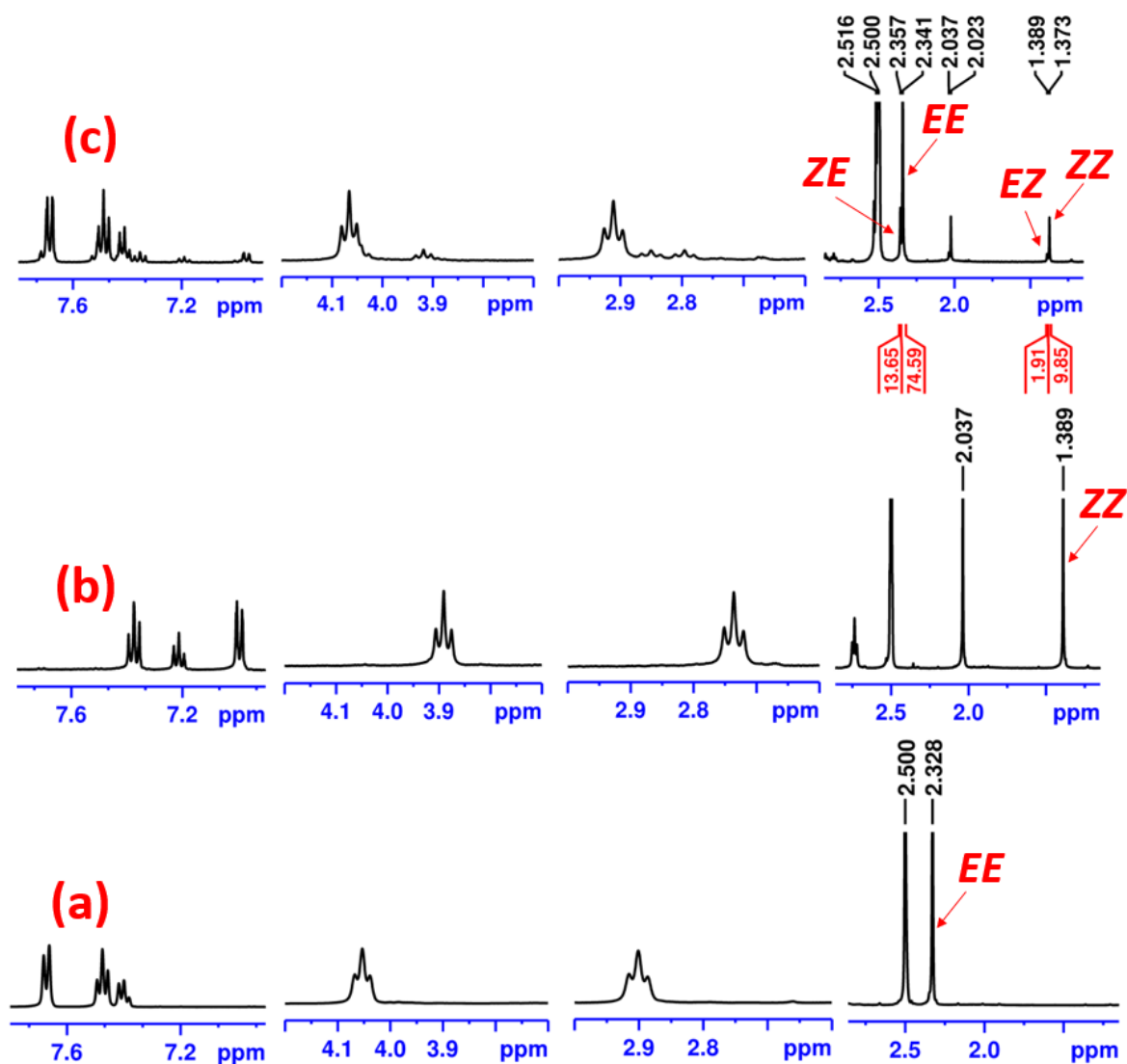
Figure S7-3: Analysis of photoswitching and estimation of PSS composition using ^{1}H-NMR spectroscopic studies of **L3** in d6-DMSO (5.5 mM) (a) before irradiation; (b) after irradiation at 365 nm; (c) after irradiation at 470 nm. (The normalized integral values corresponding to methyl signal was used for the estimation of PSS composition.)
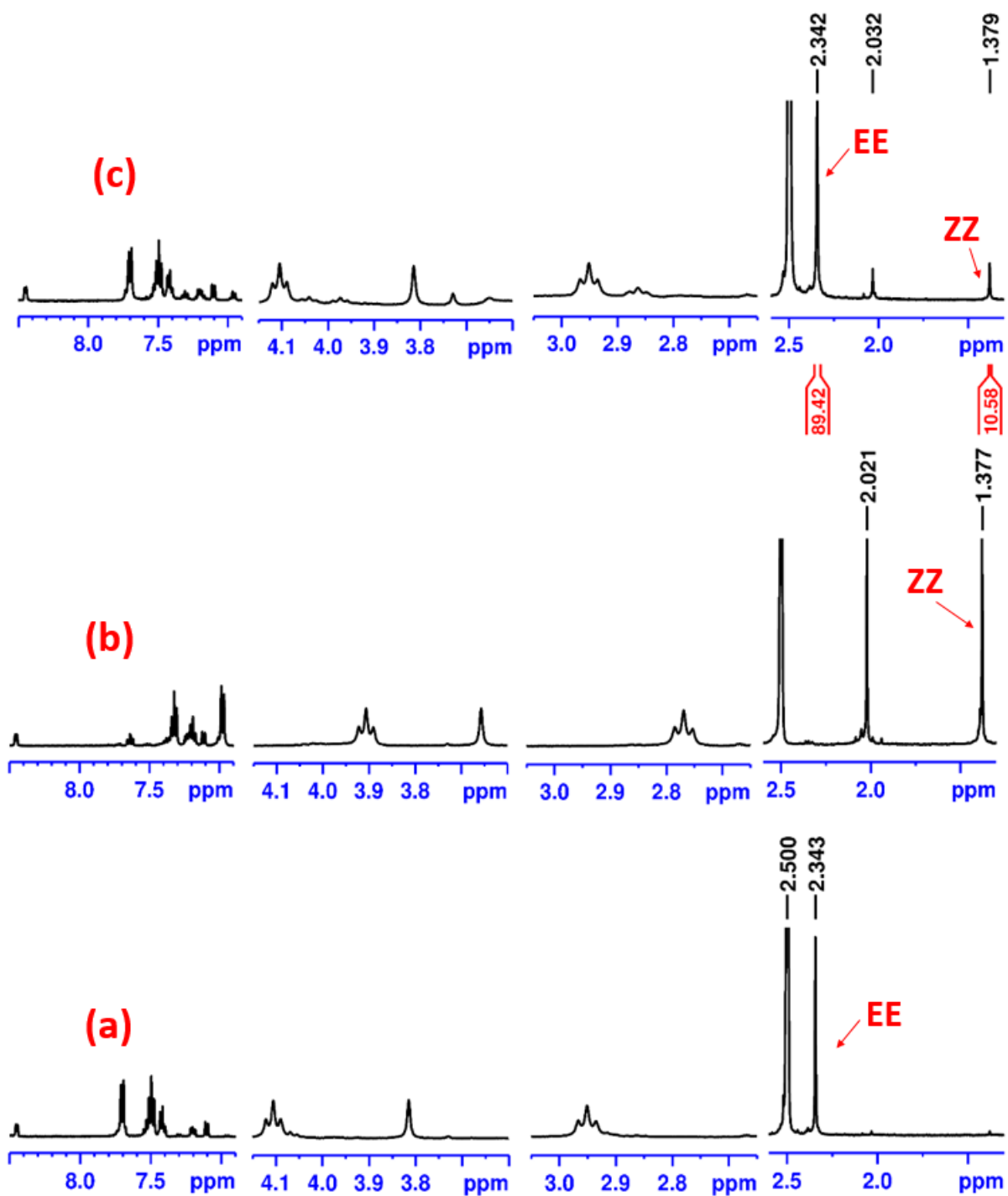
Table S7-1. Quantification of photoisomers at photostationary state by ^{1}H NMR

S. No.	Compound	Concentration (mM)	λ (nm)	%Composition of individual isomers at PSS[a]			
				EE	*EZ*	*ZE*	*ZZ*
1.	**L1**	5	365	0	0	0	>98
			490	**75**	**2**	**14**	**10**
2.	**L2**	6	365	0	0	0	>98
			470	**62**	**4**	**17**	**15**
3.	**L3**	5.5	365	0	0	0	>98
			490	**89**	**0**	**0**	**11**

[a]PSS has been established for individual ligands through prolonged irradiation at 365 nm (forward isomerization from *EE*-isomer, represented in normal font) such that no further isomerization happens; The compositions have been deduced using ^{1}H-NMR in d6-DMSO at 25 $\pm$ 1 ^{O}C; The integral ratios of methyl protons have been used for estimation of individual isomers.
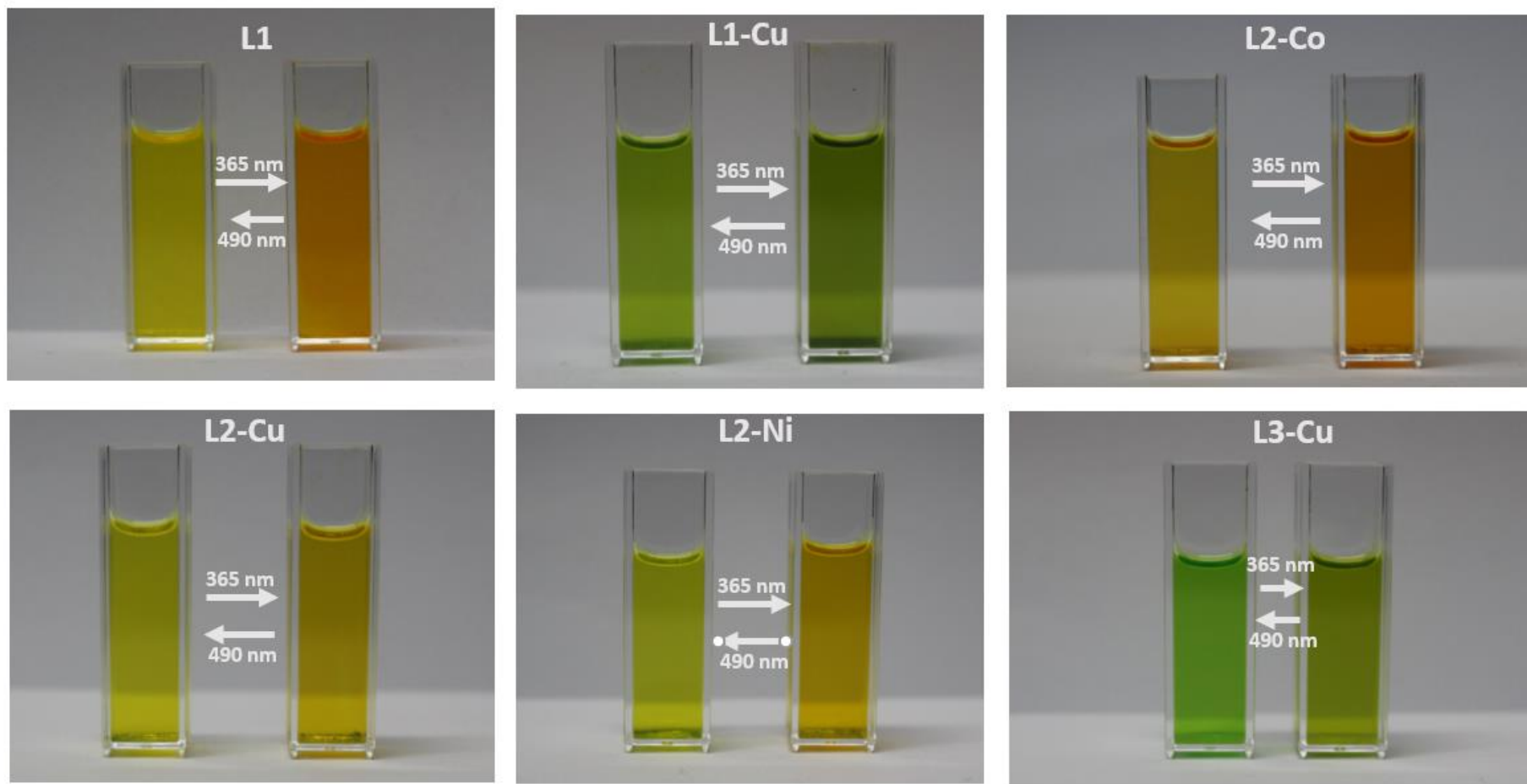
Figure S8.1: Photographs depicting the color change in acetonitrile solution of ligand **L1** (3 mM), complexes **L1-Cu** (3.1 mM), **L2-Co** (3.1 mM), **L2-Cu** (3.1 mM), **L2-Ni** (3.1 mM) and **L3-Cu** (3.1 mM) before and after irradiation.
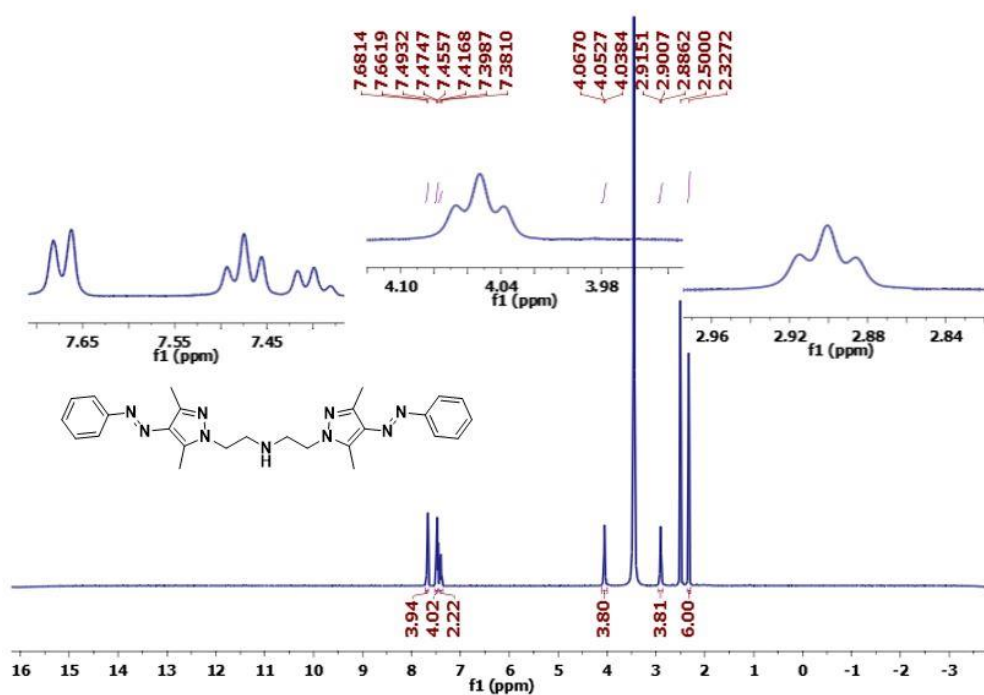
S9: ^{1}H and ^{13}C -NMR spectral data

Fig S9-1: ^{1}H NMR spectrum of bis(2-(3,5-dimethyl-4-((E)-phenyldiazenyl)-1H-pyrazol-1-yl)ethyl)amine **L1** (400 MHz, d6-DMSO)
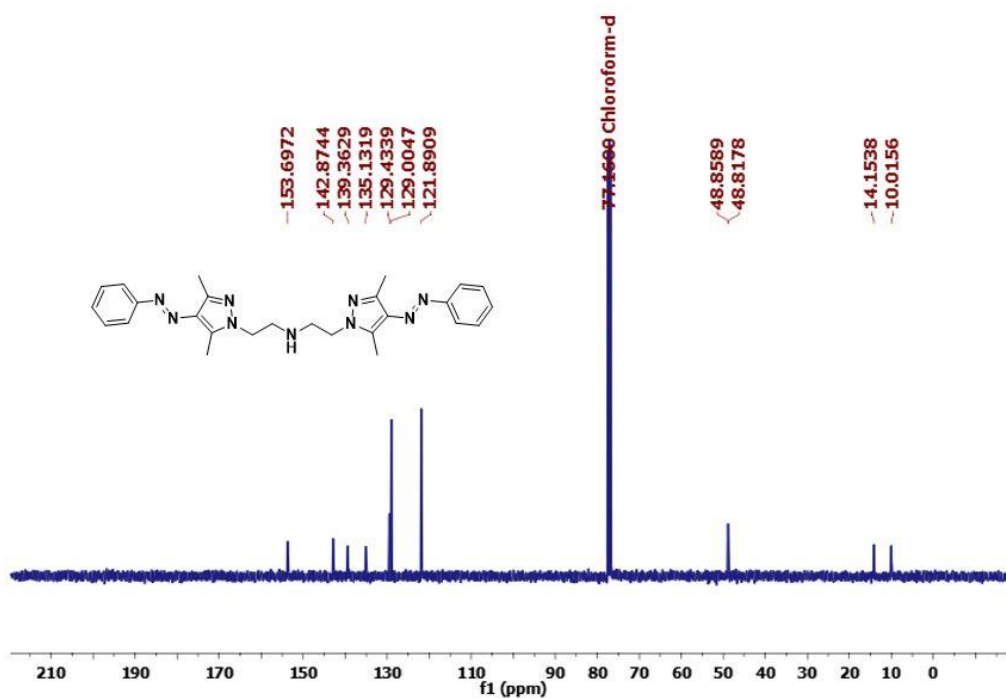

Fig S9-2: ^{13}C NMR spectrum of bis(2-(3,5-dimethyl-4-((E)-phenyldiazenyl)-1H-pyrazol-1-yl)ethyl)amine **L1** (100 MHz, CDCl$_3$)

Fig S9-3: **¹H** NMR spectrum of 2-(3,5-dimethyl-4-((E)-phenyldiazenyl)-1H-pyrazol-1-yl)-N-(2-(3,5-dimethyl-4-((E)-phenyldiazenyl)-1H-pyrazol-1-yl)ethyl)-N-methylethan-1-amine **L2** (400 MHz, d6-DMSO)

Fig S9-4: **¹³C** NMR spectrum of 2-(3,5-dimethyl-4-((E)-phenyldiazenyl)-1H-pyrazol-1-yl)-N-(2-(3,5-dimethyl-4-((E)-phenyldiazenyl)-1H-pyrazol-1-yl)ethyl)-N-methylethan-1-amine **L2** (100 MHz, CDCl₃)

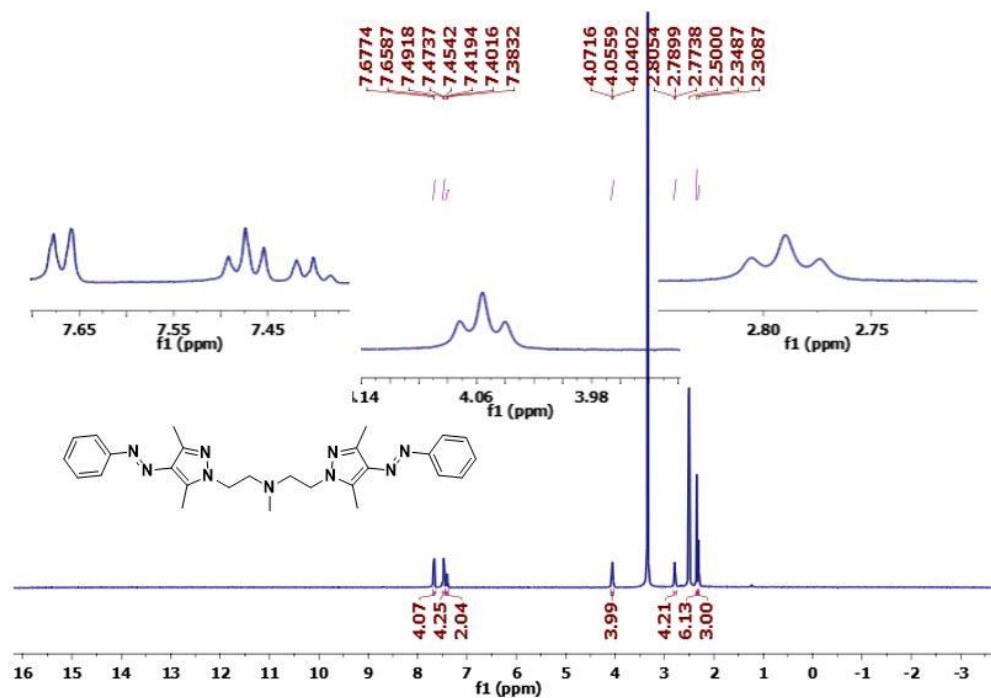**Fig S9-5:** **¹H NMR** spectrum of 2-(3,5-dimethyl-4-((E)-phenyldiazenyl)-1H-pyrazol-1-yl)-N-(2-(3,5-dimethyl-4-((E)-phenyldiazenyl)-1H-pyrazol-1-yl)ethyl)-N-(pyridin-2-ylmethyl)ethan-1-amine **L3** (400 MHz, d6-DMSO)
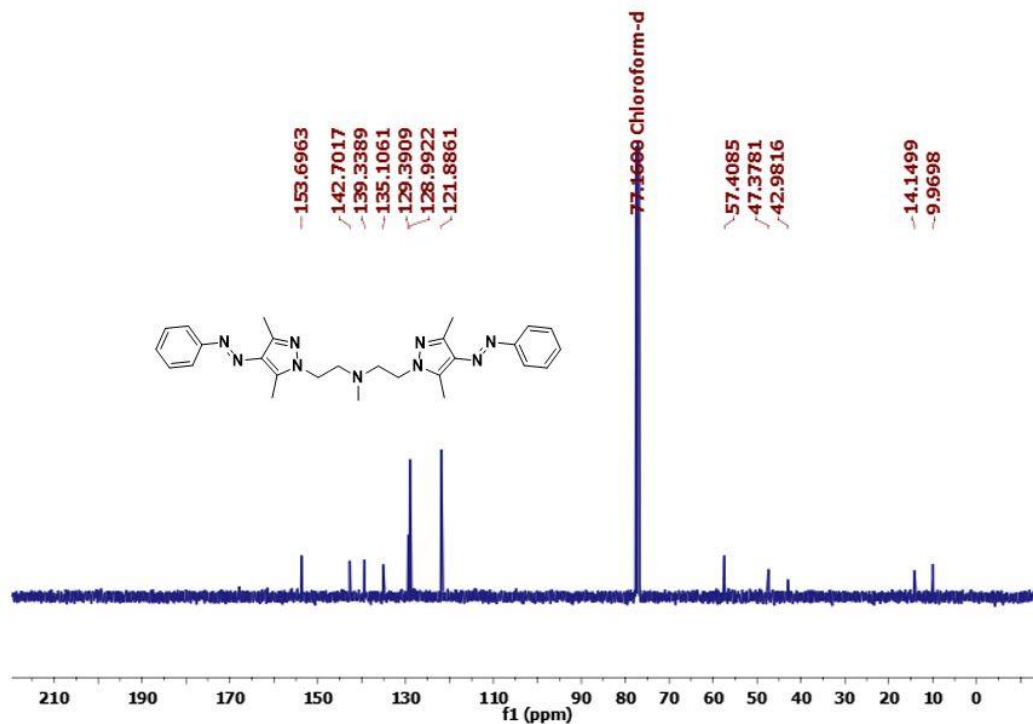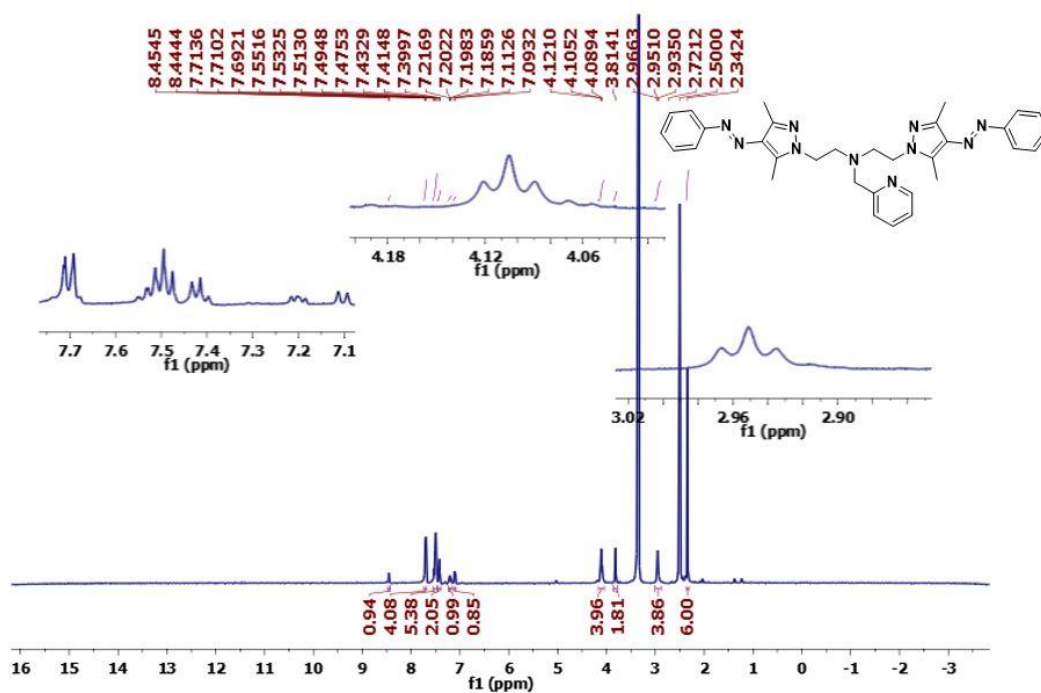

Fig S9-6: **¹³C NMR** spectrum of 2-(3,5-dimethyl-4-((E)-phenyldiazenyl)-1H-pyrazol-1-yl)-N-(2-(3,5-dimethyl-4-((E)-phenyldiazenyl)-1H-pyrazol-1-yl)ethyl)-N-(pyridin-2-ylmethyl)ethan-1-amine **L3** (100 MHz, CDCl₃)
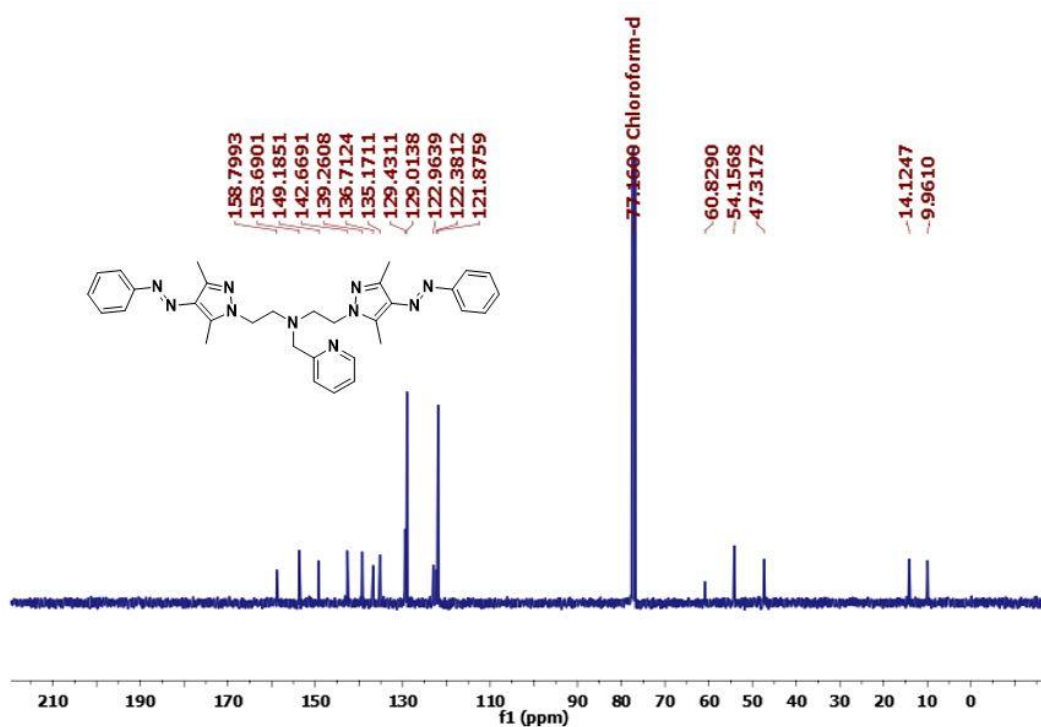
S10: References:

1. T. N. Sorell and M. R. Malachowski, Mononuclear three-coordinate copper(I) complexes: synthesis, structure, and reaction with carbon monoxide, *Inorg. Chem.,* 1983, **22**, 1883-1887.
2. J-H. Choi, N. E. Schloerer, J. Bergerb and M. H. G. Prechtl, Synthesis and characterisation of ruthenium dihydrogen complexes and their reactivity towards B–H bonds, *Dalton Trans.*, 2014, **43**, 290-299.
3. R. Herchel, Z. Dvorák, Z. Trávnícek, M. Mikuriya, F. R. Louka, F. A. Mautner and S. S. Massoud, Cobalt(II) and copper(II) covalently and non-covalently dichlorido-bridged complexes of an unsymmetrical tripodal pyrazolyl-pyridyl amine ligand: Structures, magnetism and cytotoxicity, *Inorg. Chim. Acta.*, 2016, **451**, 102–110.
4. O. V. Dolomanov, L. J. Bourhis, R. J. Gildea, J. A. K. Howard and H. Puschmann, OLEX2: a complete structure solution, refinement and analysis program, *J. Appl. Crystallogr.,* 2009, **42**, 339-341.
5. G. M. Sheldrick, SHELXT - Integrated space-group and crystal-structure determination, *Acta Cryst.* A, 2015, **71**, 3-8.
6. E. N. Cho, D. Zhitomirsky, G. G. D. Han, Y. Liu and J. C. Grossman, Molecularly Engineered Azobenzene Derivatives for High Energy Density Solid-State Solar Thermal Fuels, *ACS Appl. Mater. Interfaces*, 2017, **9,** 8679-8687.
7. S. Devi, A. K. Gaur, D. Gupta, M. Saraswat and S. Venkataramani, Tripodal N-Functionalized Arylazo-3,5-dimethylpyrazole Derivatives of Trimesic Acid: Photochromic Materials for Rewritable Imaging Applications, *ChemPhotoChem*, 2018, **2**, 806-810.